ABSTRACT

HAN, CHENGBO. *Ab Initio* Studies of Graphene Nanoflakes and Phenylacetylene Self-Assembly on Au(111) Surface. (Under the direction of Dr. Jerry Bernholc.)

This dissertation focuses on the first principles simulations of the structures of surface adsorption complexes observed by scanning tunnelling microscopy (STM). We aim to identify the properties of adsorbates and the interactions between the adsorbates and the substrates. Our simulation results identify graphene vertex effects, in addition to the well-known effect from perfect graphene edges. In collaboration of the experimentalists, we investigate the phenylacetylene molecule adsorption geometries on Au(111) surface, resolving the atomic structures of the hexamer cluster and the well-ordered self-assembled monolayer. Those results clarify the interactions within this specific adsorbate-substrate system. The collaboration with experimentalist provides a direct confirmation of our results. Further investigation can be guided on similar systems.

For the graphene nanoflakes and nanoribbons, we simulate STM images of graphene nanoflakes and nanoribbons with both zigzag and armchair edges, using the real-space multigrid method and density functional theory. Our results explain several STM patterns seen in experiments, such as triangular and hexagonal STM superstructures for different shapes of flakes. We also find that localization of edge states in zigzag flakes depends on the interior angle between two edges. Armchair edges could have localized states due to bond length relaxation at edges.

In collaboration with experiment, we discovered supramolecular self-assembly of π-conjugated hydrocarbons *via* 2D cooperative CH/π interaction. By *ab initio* simulation, we revealed the atomic structure of the experimental observations and studied the character of CH/π bonding. The obtained STM image agrees with the experimental image satisfactorily. By simulations with and without the substrate, we show that the Au(111) substrate selects the ground state geometry and the adsorption site of the hexamer self-assembled cluster. We propose that a different self-assembly pattern might be present on different metal surfaces, depending on the interplay between intermolecular CH/π bonds and the interfacial interactions of the phenylacetylene-substrate system. This may lead to discovery of other 2D self-assembly pattern originating from the CH/π bond.

We calculated adsorption geometries for a single phenylacetylene molecule on Au(111) surface, considering both physisorption and chemisorption. Our results indicate that the adsorption is the most stable when the phenylacetylene molecule is chemisorbed on the Au(111) surface. The monolayer structure of a chemisorbed molecule leads to a very similar simulated STM image as in the experiment. We propose that the phenylacetylene molecule can transit between a flat-flying physisorbed structure and stable chemisorbed monolayers. Qualitative agreement

between this proposal and the experimental observations is demonstrated. Based on the preceding results, a controllable, localized, non-thermal self-assembly procedure is presented in combination with experimental justification.

Ab Initio Studies of Graphene Nanoflakes and Phenylacetylene Self-Assembly on Au(111) Surface

by
Chengbo Han

A dissertation submitted to the Graduate Faculty of
North Carolina State University
in partial fulfillment of the
requirements for the Degree of
Doctor of Philosophy

Physics

Raleigh, North Carolina

2013

APPROVED BY:

Dr. Wenchang Lu	Dr. Daniel Dougherty
Dr. Zhilin Li	Dr. Jerry Bernholc Chair of Advisory Committee

DEDICATION

To my parents and my wife.

BIOGRAPHY

Chengbo Han was born in December 1984 in Fuxian, Shaan'xi Province, China. He and his family moved to Puyang in Henan Province when he was three years old, since his father got a job there. One year later, they moved to LanKao, a remote town, and stayed there until he was twelve. Once again due to his father's job changes, they got back to Puyang and stayed there until now. The middle and high school years were just like other children in China, filled up with homework and exams. After the National College Entrance Examination, he was admitted in Harbin Institute of Technology, majoring in Optical Information Science and Technology. In pursuit of a higher education, he came to the United States and studied Computational Physics in Prof. Jerry Bernholc's group in North Carolina State University. Research by itself was never an easy job. Still, in his spare time , he managed to acquire a Master degree in Computer Science and pass the first two exams of the Chartered Financial Analyst. Another important status change was that he got married on the Christmas of his fifth Ph.D. year. The overall Ph.D. life was a very demanding but yet still manageable experience.

ACKNOWLEDGEMENTS

First of all, I am very grateful to be a Ph.D. student of my advisor Prof. Jerry Bernholc. He provided me unique experiences in the state-of-the-art simulation technologies, and helped me to get access to the most advanced simulation facilities and personals. His words were always filled up with wisdom and enlightened me from time to time. His generous financial support granted me sufficient time to focus on research and self-enrichments. I also owe many thanks to Dr. Wenchang Lu for his daily guidance and advice in research and life. The research experience with them is both challenging and rewarding.

I am very gratefully for the help from our collaborators in Oak Ridge National Laboratory, Qing Li, Scott Horton, Miguel Fuentes-Cabrera, Bobby G. Sumpter, Petro Maksymovych and Minghu Pan. They provided valuable inputs and discussions for the project and guided me through the collaborative research. It is a very happy time to work with them.

I am happy to thank my friends and workmates: Liping Yu, Xin Li, Bikan Tan, Minyi Zhu, Shi Guo, Yan Li, Vivek Ranjan and Frisco Rose. It is such an enjoyable experience with them around. They helped me in both research and life.

Finally, I would like to thank my parents far away in China, my wife who brought much happiness to me and all the friends that have helped me.

TABLE OF CONTENTS

LIST OF TABLES

LIST OF FIGURES

Chapter 1

Introduction

Surface science is of key importance in modern technology. Exploring new materials and novel applications might lead to progress similar to the rise of IT industry. Driven by the desire to pattern surfaces beyond lithographic limitation, to sense environmental changes at single molecule limit and to acquire conducting materials with tunable electronic properties, both academic and industrial researchers keep exploring new materials and trying with different combinations of materials at surface.

To reach quantitative conclusions, model systems are widely used in materials science research. Among many models, the flat surface geometry and few layers of adsorbates are the most popular. The essentials of surface influence over an adsorbate can be most easily understood when the surface is flat, that is of a low Miller index. This simplifies the problem by removing the effect of steps or disorder on the surface. Regarding to the quantum effect that lies at the core of today's nanotechnology, it is demonstrated the best when the adsorbates are of single-layer thickness. With a few layers of stacking, the adsorbates will quickly recover bulk crystallographic properties.

The physical system of interest in this thesis is the π-conjugated adsorbates on low-index surfaces of either a doped semiconductor or a metal in high vacuum. The target material systems are the graphene on highly doped Si(100)2×1-H substrate and phenyl acetylene on the Au(111) surface.

First discovered in 2004 and granted a Nobel Prize in 2007, graphene is the ideal platform for future nanoelectronic devices. It is inherently compatible with current lithographic processes, has electron mobility two orders of magnitude greater than that of silicon devices and is able to conduct heat two times faster than diamond. Understanding of graphene, especially of the edge states, is important to applications.

Lyding and co-workers [1] used an in-situ technique to deposit graphene flakes onto highly-doped Si(100)2×1-H substrate. They observed that nanometer-size graphene flakes have differ-

ent Scanning Tunneling Microscopy (STM) patterns from a micrometer-size sample. The edge structure is likely to contribute to the novel patterns, but due to quickly decreasing STM resolution near the graphene edge step, no clear conclusions can be drawn. In a separate paper [2], Lyding *et al.* found the during STM scanning the graphene film was pushed down by about 0.5 Å. This makes the interpretation of the STM even harder with stronger interaction between the graphene sample and the substrate.

For studies of organic–metal interfaces, π-conjugated molecules have long been a basic model that is of key importance to various electronic and energy–related applications. Aromatic molecules like benzene and pentacene are the most important examples in this field. However, flat-lying aromatic molecules on surface are inert and repulsive to each other. This prevents aromatic groups form meaningful structures for applications.

Activation of aromatic molecules by invoking ethyne groups (–C≡C–H) as the attractive center is an appealing alternative to get ordered structures. The alkyne group (–C≡C–H) on phenyl acetylene can serve as both a Lewis acid and a base, *i.e.*, hydrogen donor and accepter, to form CH/π bond. The alkyne group has the directional and cooperative nature needed for typical self-assembly. With proper preparation, the alkyne group can also be reactive to the surface.

In self-assembly systems, the process of assembly usually influences the ultimate structure to a large extent. Certain chemical reactions can only take place at a high temperature, although the products lower the total energy of the reactants. Likewise, the adsorption process has a similar barrier. Simple adsorbates, like metal atoms, adopt the most stable adsorption structure. But for self-assembly structures, it is not necessary to always achieve the thermodynamically global minimum, but rather reach a semi-stable structure.

The preparation process is important, but it is always true that only stable and geometrically rigid structures can be used in real molecular applications. Instead of directly dealing with the dynamic process, in this thesis work, we focus on the properties of stable adsorption structures. Those structures typically appeared after post-annealing. Some preliminary results for the reaction and diffusion barriers are also included to guide future research in the dynamic processes.

The precise adsorption geometry of the adsorbate on the surface is central to the physical properties of the adsorption complex. STM is the primary tool to probe the surface geometry and identify the electronic states at nanometer scale. However, with limited resolution, the atomic configuration in many cases cannot be interpreted from the experimental STM image directly.

Further more, many physics properties are characterized by specific electronic states. Despite the capability of spectroscopy, STM measurements generally cannot identify individual electronic states of the aromatic molecule because of strong coupling to the metal surface states.

At those points, quantitative simulation plays a central role in determining and understanding the experimental observations. Density Functional Theory (DFT) is one of the most widely accepted first-principles simulation methods. Given atomic positions and the atomic numbers, DFT calculates the properties of the physical system from quantum laws without empirical parameters. Many successful applications proved the effectiveness of DFT for the ground state properties of well–bonded systems. With proper density–functional corrections, like the van der Waals correction, DFT can also accurately describe the weakly-bonded systems described in this thesis.

The computational tools used in this work are state-of-the-art DFT solver packages: Real-space Multi-Grid (RMG) code, Plane-Wave Self-Consistent Field (PWscf) simulation package, and Vienna Ab-initio Simulation Package (VASP). A post-process code is developed to enable simulating the STM images. Using one of the most powerful supercomputers in the world and a handful utilities in automation scripts, we are able to perform many of computations in parallel and finish them within my limited Ph.D. research time.

The rest of the thesis is organized as follows: Chapter 2 outlines the DFT framework used in the thesis. Chapter 3 studies interference patterns near vertices in graphene nano-structures. Chapter 4 investigates the self-assembly structure of phenyl-acetylene on the Au(111) surface. Chapter 5 explores tip-bias-enabled structural transition of phenyl-acetylene on Au(111). Both Chapter 4 and 5 are heavily interwoven with experimental procedures and observations.

Chapter 2

Methodology

In this thesis, the primary simulation methodology for various materials is the state-of-the-art Density Functional Theory (DFT). Many good reviews have been published [3–9]. This chapter illustrates the practice and the concepts underlying the DFT.

The concepts in DFT show themselves the best in the context of its historical development , especially those ones that were introduced right before DFT. By reviewing these ancestor methodologies, we notice that there are still much room left to deepen the understanding of the electron system and to improve the efficiency of the computation.

2.1 Pre-Density Functional Calculations

In the microscopic world, particles like electrons and ions are best described in the mathematical form of waves. The Schröodinger equation, the law that governs this microscopic world, takes the form of Hamilton-Jacobi equation, where the whole system is evolving to the ground state that has the global minimum energy. In term of physics quantities, the Hamiltonian is corresponding to the total energy of a quantum system. It has the fundamental role in describing the quantum system. For a ground state condensed matter study, it is sufficient to use a time-independent non-relativistic Schrödinger equation as

$$\hat{H}|\Psi\rangle = E|\Psi\rangle. \tag{2.1}$$

$\hat{H}$ is the Hamiltonian operator. E and $|\Psi\rangle$ are the eigenvalue and the eigenstate of $\hat{H}$, respectively. The ground state of a material is the eigenstate of the Hamiltonian that has the smallest eigenvalue. This thesis work is on non-magnetic materials, and the spin interaction does not need to be considered.

The the many-body wave function $|\Psi\rangle$ is a function of electronic positions r_i and ionic

positions R_i,

$$|\Psi\rangle = \Psi(\mathbf{r}_1, \mathbf{r}_2, \ldots, \mathbf{r}_{N_e}; \mathbf{R}_1, \mathbf{R}_2, \ldots, \mathbf{R}_{N_a}), \tag{2.2}$$

where N_e is the number of electrons, and N_a is the number of nuclei.

A full interaction description of the condensed matter system requires many-body formalism. The many-body Hamiltonian $\hat{H}$ is

$$\begin{aligned} \hat{H} &= \hat{T}_e + \hat{T}_n + \hat{V}_{ee} + \hat{V}_{ne} + \hat{V}_{II} \\ &= -\frac{\hbar^2}{2m_e}\sum_i \nabla_i^2 - \sum_I \frac{\hbar^2}{2M_I}\nabla_I^2 + \frac{1}{2}\sum_i \sum_{j\neq i} \frac{e^2}{|\mathbf{r}_i - \mathbf{r}_j|} \\ &\quad - \sum_i \sum_I \frac{Z_I e^2}{|\mathbf{r}_i - \mathbf{R}_I|} + \frac{1}{2}\sum_I \sum_{J\neq I} \frac{Z_I Z_J e^2}{|\mathbf{R}_I - \mathbf{R}_J|}. \end{aligned} \tag{2.3}$$

$\hat{T}_e$ and $\hat{T}_n$ are kinetic energy operators, representing electron and nuclei, respectively. $\hat{V}_{ee}$, $\hat{V}_{ne}$ and $\hat{V}_{II}$ are potential operators describing the electron-electron, electron-nucleus and nucleus-nucleus Coulomb interactions. $\hat{V}_{ne}$ is also known as the positive background of the electron system. m_e is the electron mass. Z_I and M_I are the atomic number and the nucleus mass of the atom at the position R_I.

Although the many-body Hamiltonian is straightforward to build, it is an impossible task to get the exact solution even for a few electrons. However, many of the real materials science studies inevitably have at least hundreds of electrons. Even using numerical methods, to search for the solutions in a space of hundreds degrees of freedom is a horribly complicated task. To get quantitative results, we need good approximations.

2.1.1 Born-Oppenheimer Approximation

One of the terms in the Eq. 2.3 is small and can be readily taken off. This is the kinetic energy of the nuclei. M_I is 10^4 times the m_e, and the interaction between them has the same order of magnitude. This implies electrons respond to the nuclei motion instantaneously and at the same time scale the electrons relax to the instantaneous ground state. In the Born-Oppenheimer approximation [10] (also known as the adiabatic approximation), the positions of the nuclei are parameters used in the positive background. The many-body wave function is separated into the electronic wave function and the nuclear wave function. The $\hat{T}_I$ is omitted in the Hamiltonian, as the R_I are taken as fixed. It is a good approximation for many physical systems. The focus of the condensed matter system is then shifted to the electronic system:

$$\hat{H}|\Phi\rangle = E|\Phi\rangle, \tag{2.4}$$

where

$$\hat{H} = \hat{T}_e + \hat{V}_{ee} + \hat{V}_{ne} + \hat{V}_{II}, \tag{2.5}$$

$$|\Phi\rangle = \Phi(\mathbf{r}_1, \mathbf{r}_2, \ldots, \mathbf{r}_{N_e}). \tag{2.6}$$

The Coulomb interaction in an extended system can only be finite if the overall system is neutral. Therefore, even though the ionic motion is separated from the electron gas, the nuclei are needed to neutralize the electron system.

2.1.2 Independent-Electron Approximation

Many-body interaction is very complex, especially when more than two particles can interact with each other at the same time. To reduce the complexity, the full interactions between the participants of the Hamiltonian are approximated as simplified interactions in an auxiliary system. The most common one is the independent-electron approximation, where the electrons are uncorrelated between each other.

Two wave-function-based variational approaches are commonly used in this approximation: the Hartree-like method [11] and the Hartree-Fock method [12]. In either case, the many-body wave function for electrons is represented as certain combinations of single-electron wave functions.

Hartree-like method

The Hartree-like method utilizes the non-interacting-electron approximation. It constructs an effective potential to represent the interactions between electrons. The accuracy is then dependent on the approximations made in the effective potential. This method was first demonstrated by Hartree, calculating the orbital for each electron in an effective potential composed of the other electrons and the nucleus. In his work, the effective potential depends on the electronic orbitals other than the one in current calculation. Later development of "mean field theory" dictates that all the electrons are moving in the same average effective potential produced by all the charged particles. This greatly reduced the computational cost (from $N!$ interactions to N interactions through the effective potential), but introduced the spurious self-interaction, that is the electron feels the Coulomb potential from itself. Therefore, an additional correction term is needed.

The non-interacting model is the ancestor of many modern computational methods. Density Functional Theory explicitly takes the same shape as the Hartree-like equations.

Hartree-Fock Method

The Hartree-Fock method explicitly includes the pair-wise electron-electron Coulomb interaction in the Hamiltonian, but neglects the interactions beyond the two-body problem. The full many-body wave function is approximated with Slater determinant to maintain the required anti-symmetric properties of Fermions. The orthogonal basis set used in the Slater determinant is analogues to a set of single-electron orbitals. The total energy is minimized for all the degrees of freedom in the wave function, with the constraint that the wave function is anti-symmetric and the number of electrons is conserved.

In the above formalism, the electron-electron interaction is described explicitly as the classical electrostatic Hartree energy and the non-classical exchange energy. The Hartree energy is

$$E_{Hartree} = \frac{1}{2} \int \mathrm{d}\mathbf{r}\, \mathrm{d}\mathbf{r}' \frac{n(\mathbf{r})n(\mathbf{r}')}{|\mathbf{r} - \mathbf{r}'|}. \tag{2.7}$$

The exchange energy is

$$E_x = -\frac{e^2}{2} \sum_{i,j} \int \mathrm{d}\mathbf{r}\, \mathrm{d}\mathbf{r}' \frac{\phi_i^*(\mathbf{r})\phi_j^*(\mathbf{r}')\phi_i(\mathbf{r}')\phi_j(\mathbf{r})}{|\mathbf{r} - \mathbf{r}'|}. \tag{2.8}$$

$E_{Hartree}$ has the spurious self-interaction, but it is cancelled by the exchange energy term exactly. The exchange energy is lowering the total energy due to the electron interaction with the positive exchange hole surrounding it. This effect originates from the anti-symmetry property of the Fermion.

The Hartree-Fock approximation can be systematically improved by adding more correlation terms, and many approximation are widely used in quantum chemistry and simulation of spectra, such as the configuration interaction. But like other wave-function-based computations, the calculation cost grows fast as the number of electrons increases. Typically, the Hartree-Fock method is only used for small systems with no more than 100 atoms.

2.1.3 Density Functional

Homogeneous Electron Gas

The homogeneous electron gas, also known as Jellium or uniform electron gas [4], is an interacting electron system that has a uniform positive background, and the electron density is also uniform throughout the space. The homogeneous electron gas is the simplest model because all the physical properties are completely determined by the charge density. It serves as the basic system to study the exchange-correlation interactions in the electron system. This model removes the atomic structure, and focuses on the inherent properties of the electron interactions. The homogeneous gas has a limited interpretation to the electronic states in a metal, where the

valence electrons are weakly bonded. Based on the non-interacting homogeneous electron gas model, the Fermi liquid theory successfully describes the non-superconducting state of metals.

Thomas-Fermi-Dirac Model

The first demonstration of a theory with a density functional for a many-particle system was in 1927 by Thomas [13] and Fermi [14]. They both employed a crude approximation that the kinetic term of the Hamiltonian is expressed as a functional of the charge density. The electron interaction is approximated with the homogeneous gas model in a mean-field approach. The exchange and correlation of the interacting electron system was totally ignored at that time . Later in 1930, Dirac formulated the exchange interaction in a homogeneous gas [15]. In terms of the computational cost, the density functional expression of the Hamiltonian is a success. The solution searching now has only 3 degrees of freedom, compared to the 3 degrees of freedom for each single-electron orbital. However, the approximation made in the Hamiltonian, especially in the kinetic energy term, misses the behaviour of many valence electron properties that are critical to materials simulation. Nevertheless, Thomas-Fermi-Dirac model opened the door to the Density Functional Theory.

2.2 Density Functional Theory

Density Functional Theory is one of the fundamental advances in modern condensed matter physics, not only in practical usage to understand materials and chemistry processes, but also in understanding the electronic behaviour in real matter. It builds on two fundamental components: the Hohenberg-Kohn theorem [16] and the Kohn–Sham equation [17] .

2.2.1 Hohenberg-Kohn Theorem

The Hohenberg-Kohn theorem [16] proves that

1 For any interacting particle system, the external field $V_{ext}(\mathbf{r})$ is uniquely determined by the ground state density $n(\mathbf{r})$, except for an additive constant.

2 For any external potential, the total energy $E[n]$ can be defined in terms of the density $n(\mathbf{r})$ as a universally valid functional. The ground state is the state that represents the global minimum of the total energy functional. The charge density that minimizes the total energy functional is the ground state charge density.

$V_{ext}(\mathbf{r})$ is defined as external potential acting on the electronic system. Often, $V_{ext}(\mathbf{r}) = \langle\Phi|\hat{V}_{en}|\Phi\rangle$. The ground state charge density $n(\mathbf{r})$ is defined as

$$n(\mathbf{r}) = N \int \mathrm{d}^3 r_2 \, \mathrm{d}^3 r_3 \ldots \, \mathrm{d}^3 r_{N_e} |\Phi(\mathbf{r}_1, \mathbf{r}2, \ldots, \mathbf{r}_{N_e})|^2. \tag{2.9}$$

Simple Proof of Theorem 1: Assume that there is a ground state charge density $n_0(\mathbf{r})$, which has two corresponding external potentials $V_{ext}(\mathbf{r})$ and $V'_{ext}(\mathbf{r})$. These two external potentials differ from each other by more than an additive constant. Thus, they have two sets of Hamiltonians, $\hat{H}$ and $\hat{H}'$, and two ground state wave functions $|\Phi_0\rangle$ and $|\Phi'_0\rangle$ and two ground state energies $E_0 = \langle\Phi_0|\hat{H}|\Phi_0\rangle$ and $E'_0 = \langle\Phi'_0|\hat{H}'|\Phi'_0\rangle$.

For a usual physical systems the ground state is unique and has the minimum ground state energy. Therefore,

$$\begin{aligned} \langle\Phi_0|\hat{H}|\Phi_0\rangle &< \langle\Phi'_0|\hat{H}|\Phi'_0\rangle = \langle\Phi'_0|\hat{H}'|\Phi'_0\rangle + \langle\Phi'_0|\hat{H} - \hat{H}'|\Phi'_0\rangle \\ E_0 &< E'_0 + \int \mathrm{d}^3 r n_0(r) \left[V_{ext}(\mathbf{r}) - V'_{ext}(\mathbf{r})\right] \end{aligned} \tag{2.10}$$

and

$$\begin{aligned} \langle\Phi'_0|\hat{H}'|\Phi'_0\rangle &< \langle\Phi_0|\hat{H}'|\Phi_0\rangle = \langle\Phi_0|\hat{H}|\Phi_0\rangle + \langle\Phi_0|\hat{H}' - \hat{H}|\Phi_0\rangle \\ E'_0 &< E_0 + \int \mathrm{d}^3 r n_0(\mathbf{r}) \left[V'_{ext}(\mathbf{r}) - V_{ext}(\mathbf{r})\right]. \end{aligned} \tag{2.11}$$

Addition of the Eq. 2.10 and Eq. 2.11 leads to a conflict, therefore the ground state density is unique.

Proof of Theorem 2: The universal valid electronic Hamiltonian operator $\hat{F}$ is

$$\hat{F} = \hat{T}_e + \hat{V}_{ee}. \tag{2.12}$$

The total energy functional is then

$$E[n(\mathbf{r})] = T_e[n(\mathbf{r})] + E_{ee}[n(\mathbf{r})] + \int V_{ext}(\mathbf{r}) n(\mathbf{r}) \, \mathrm{d}\mathbf{r}. \tag{2.13}$$

Here we omit the electrostatic ion-ion interaction E_{II} term in the total energy $E[n(\mathbf{r})]$, since it is only a constant in the current problem.

By theorem 1 we know that the $n(\mathbf{r})$ and the $V_{ext}(\mathbf{r})$ have one-to-one relationship. Introduce Φ^n_{min} that generates the charge density $n(\mathbf{r})$ and minimizes $\hat{F}$ for all possible choices of $\Phi(\mathbf{r})$.

Then we have

$$\begin{aligned}\min_{n(\mathbf{r})} E[n(\mathbf{r})] &= \langle\Phi^n_{min}|\hat{F}|\Phi^n_{min}\rangle + \int \mathrm{d}^3 r\, V_{ext}(\mathbf{r})n(\mathbf{r}) \\ &= \langle\Phi^n_{min}|\hat{F} + V_{ext}(\mathbf{r})|\Phi^n_{min}\rangle \\ &\leq \langle\Phi_{ground}|\hat{H}|\Phi_{ground}\rangle = E_{ground}.\end{aligned}$$

The ground state can be obtained variationally, with the charge density that minimizes the functional $E[n(\mathbf{r})]$. The ground state energy E_{ground} is the minimum value of the functional.

The Hohenberg-Kohn theorem is exact for many-body systems. It illustrates the relationship between the ground state charge density and the external potential without making approximations in the expression of the Hamiltonian and the energy functional. However, it has limited practical usage as it does not provide a formalism to recall the Hamiltonian or the energy in terms of the charge density. In fact, to evaluate the kinetic energy accurately, the laplacian operator has to operate explicitly on the wave function instead of the charge density $n(\mathbf{r})$. Further, thinking of the Pauli principle that forbids two electrons to occupy the same electronic state, it has no obvious relations to the charge density in any simple fashion. Regarding the number of electrons, the kinetic energy and the potentials vary in a non-analytical way for a real system. This further prevents the invention of an analytical expression for the energy density functional.

2.2.2 Kohn-Sham Ansatz

Without rigorous proof, the Kohn-Sham ansatz [17] proposes that the ground state density for a many-body system can be represented by the ground state density of an auxiliary system composed of non-interacting particles.

In the Kohn-Sham DFT, the electron-electron interaction is written in terms of the Hartree energy, Eq. 2.7. In this classical expression, the electron feels the electron potential generated by itself. The effective potential needs to cancel this spurious self-interaction. In Kohn-Sham DFT, this cancellation is not exact. In a near homogeneous system (like metal), the self-interaction is negligible. However, in a very inhomogeneous system (like an isolated atom), the error is expected to be larger. However, the error due to self-interaction is not large enough to spoil the success of DFT in many practical simulations.

The non-classical electrostatic interaction due to the property of the many-body Fermion system is not included in the Hartree term. Together with the difference between the kinetic energies of the many-body system and the auxiliary system, E_{xc} is implicitly defined as

$$E_{xc} = T_e - T_s + E_{ee} - E_{Hartree}, \tag{2.14}$$

where T_s is the kinetic energy of the auxiliary electron system. This is the formal definition of the exchange correlation energy.

The single electron orbitals in the non-interacting system obey the orthonormal constraints

$$\langle \phi_i | \phi_j \rangle = \delta_{i,j}. \tag{2.15}$$

The charge density is

$$n(\mathbf{r}) = \sum_{i=1}^{N} n_i |\phi_i(\mathbf{r})|^2, \tag{2.16}$$

where n_i is the occupation number of the electron state i.

Subject to the total charge conservation $\int \mathrm{d}\mathbf{r} n(\mathbf{r}) = N$, and following the definition of E_{xc} in Eq. 2.14, variation of the Eq. 2.13 gives

$$\delta_i \left[T_s[n(\mathbf{r})] + E_{Hartree}[n(\mathbf{r})] + E_{xc}[n(\mathbf{r})] + \int V_{ext}(\mathbf{r}) n(\mathbf{r}) - \varepsilon_i \left(\int \mathrm{d}\mathbf{r} n(\mathbf{r}) - N \right) \right] = 0. \tag{2.17}$$

Variation of Eq. 2.17 with respect to the single electron wave function $\phi(\mathbf{r})$ gives

$$\left(-\frac{\hbar^2}{2m_e} \nabla_i^2 + V_{Hartree}(\mathbf{r}) + V_{xc}(\mathbf{r}) + V_{ext}(\mathbf{r}) \right) \phi_i(\mathbf{r}) = \varepsilon_i n_i \phi_i(\mathbf{r}), \tag{2.18}$$

with

$$V_{Hartree}(\mathbf{r}) = \frac{\delta E_{Hartree}}{\delta n(\mathbf{r})} = \int \mathrm{d}\mathbf{r}' \frac{n(\mathbf{r}')}{|\mathbf{r} - \mathbf{r}'|}, \tag{2.19}$$

$$V_{xc}(\mathbf{r}) = \frac{\delta E_{xc}}{\delta n(\mathbf{r})}, \tag{2.20}$$

$$V_{ext}(\mathbf{r}) = -\sum_I \frac{Z_I}{|\mathbf{r} - \mathbf{R}_I|}. \tag{2.21}$$

And the three potential terms are also known as Kohn-Sham effective potential

$$V_{KS} = V_{Hartree} + V_{xc} + V_{ext}. \tag{2.22}$$

An eigenvalue for a full many-body system is the energy needed to add or remove one electron from the corresponding electron states. But in Kohn-Sham DFT, the eigenvalues from the auxiliary system do not have the same interpretations. The only exception is that the eigenvalue for the highest occupied state, if calculated with an exact functional, is the minus of the ionization energy.

Under the fractional occupation assumption of Eq. 2.16, the eigenvalue of the Kohn-Sham

DFT is defined as the derivative of the total energy in terms of the state occupation [18],

$$\varepsilon_i = \frac{\mathrm{d}E_{tot}}{\mathrm{d}n_i}. \tag{2.23}$$

In a rigorous physical sense, the Kohn-Sham eigenvalues do not have direct correspondence to the eigenvalues of the many-body system [19]. Nevertheless, the eigenvalues from Kohn-Sham DFT calculations are often used as first-order approximations to the true values.

The total energy functional of the auxiliary system can also be shown to be

$$E_{tot} = \sum_{i=1}^{N} \varepsilon_i - \frac{1}{2} \int \mathrm{d}^3 r \, \mathrm{d}^3 r \frac{n(\mathbf{r}) n(\mathbf{r}')}{|\mathbf{r} - \mathbf{r}'|} - \int \mathrm{d}^3 r V_{xc}(\mathbf{r}) n(\mathbf{r}) + E_{xc}[n(\mathbf{r})] + E_{II}. \tag{2.24}$$

The ion-ion electrostatic interaction E_{II} is defined in the same way as Eq. 2.3. The first term is the sum of the Kohn-Sham eigenvalues, where

$$\begin{aligned} \sum_{i=1}^{N} \varepsilon_i &= T_s[n(\mathbf{r})] + \int \mathrm{d}^3 r n(\mathbf{r}) V_{KS}(\mathbf{r}) \\ &= T_s[n(\mathbf{r})] + \int \mathrm{d}^3 r \, \mathrm{d}^3 r' \frac{n(\mathbf{r}) n(\mathbf{r}')}{|\mathbf{r} - \mathbf{r}'|} + \int \mathrm{d}^3 r V_{xc}(\mathbf{r}) n(\mathbf{r}) + \int \mathrm{d}^3 r n(\mathbf{r}) V_{ext}(\mathbf{r}). \end{aligned} \tag{2.25}$$

Kohn-Sham DFT utilizes a form of a Hartree-like equation, with the kinetic operator explicitly operating on the single-electron orbitals. This is a big improvement over the Thomas-Fermi-Dirac formalism, where the kinetic term is a direct functional of charge density.

Similarly to the Hartree-like approach, the effective potential in the Kohn-Sham ansatz is responsible for all the difference between the non-interacting system and the full many-body system. If we can get an exact effective potential to make up this difference, then we can get the exact ground state charge density for the many-body system. Further more, by the Hohenberg-Kohn theorem, the Hamiltonian for the many-body system is uniquely determined, within an additive constant. Therefore, the ground state properties of the interacting many-body system are determined.

Kohn-Sham DFT theory maps the full interacting many-body problem onto a non-interacting system, but this is not the only choice. An auxiliary system can incorporate certain interactions explicitly in the Hamiltonian, as long as the effective potentials can lead to the ground state charge density required in the Hohenberg-Kohn theorem. One example is the spin density functional theory [19] where the spin density is used instead of the total charge density.

The great success of Kohn-Sham DFT scheme is known from the great number of successful applications in simulation of materials properties. Together with the Local Density Approximation (LDA) and many flavours of Generalized Gradient Approximations (GGAs), DFT has

accurately predicted the ground state properties for many materials. But it fails in materials that have strongly correlated electrons or very dispersive interactions, because LDA and GGA are not able to describe them. The DFT community is thus continuously trying to improve the approximations made in the exchange-correlation functional.

In summary, Kohn-Sham DFT is a milestone in modern computational physics. It inherits the concept of single-electron system with effective potentials as in the Hartree-like equation, and the density functional idea from the Thomas-Fermi-Dirac formalism. The unexpected success led to much progress in understanding many-electron systems and a large number of practical applications in a broad area.

2.2.3 Exchange-Correlation Functional

As proposed in the original paper [17], the exchange-correlation energy is usually approximated by a local form

$$E_{xc}^{LDA} = \int \epsilon_{xc}[n] n(\mathbf{r})\, \mathrm{d}\mathbf{r}. \tag{2.26}$$

The $\epsilon_{xc}[n]$ is a local charge density functional. It is usually separated as exchange ϵ_x and correlation part ϵ_c

$$\epsilon_{xc}[n] = \epsilon_x[n] + \epsilon_c[n]. \tag{2.27}$$

The exact form for the exchange energy is known in terms of the single-electron orbitals as in the Eq. 2.8.

For typical charge densities found in condensed matter systems, the effect of the exchange and correlation is indeed mostly local [17], and can be approximated by that of the homogeneous gas. The effective potentials can also be non-local. Kohn and Sham also proposed Hartree-Fock-like non-local method to explicitly account for the exchange interaction. Some non-local, often orbital-dependent effective potentials have been developed for the DFT approach, such as meta-GGA [20] and OEP [18, 21] *etc.*

The exchange-correlation potential V_{xc} is the functional derivative of E_{xc} over the charge density $n(\mathbf{r})$.

$$V_{xc}(\mathbf{r}) = \epsilon_{xc}[n] + n(\mathbf{r}) \frac{\delta \epsilon_{xc}[n]}{\delta n(\mathbf{r})}. \tag{2.28}$$

The second term is called the response potential. It is due to change in the exchange-correlation energy with respect to the electron density. For a system with a band gap, the response potential is discontinuous, because of the energy change from the highest occupied state to the lowest unoccupied state. Thus, the exact exchange-correlation functional is obliged to take on the same discontinuity. However, the mostly used local and semi-local functionals (LDA and GGA) do not incorporate this character.

This band gap discontinuity [22, 23] leads to a further challenge in DFT. For an insulator, the exact response term leads to a discontinuity in the Kohn-Sham potential for electrons in the excited states.For this reason, in principle, the Kohn-Sham DFT cannot provide a correct band gap.

Local Density Approximation

LDA assumes that the $\epsilon_{xc}(\mathbf{r})$ functional depends only on the charge density at the point r and equals to that of the homogeneous electron gas. The E_{xc} is

$$E_{xc}^{LDA} = \int \epsilon_{xc}^{hom}[n(\mathbf{r})]n(\mathbf{r})\,\mathrm{d}\mathbf{r}. \tag{2.29}$$

The $\epsilon_{xc}^{hom}[n(\mathbf{r})]$ depends only on the charge density $n(\mathbf{r})$ at the position $\mathbf{r}$.

The homogeneous exchange energy functional $\epsilon_{xc}^{hom}[n(\mathbf{r})]$ was derived analytically by Dirac [15] in 1930 before the discovery of Kohn-Sham DFT.

$$\epsilon_x^{hom} = -\frac{3e^2}{4}\left(\frac{3}{\pi}\right)^{1/3} n^{1/3} \tag{2.30}$$

The correlation energy ϵ_c cannot be derived as the ϵ_x except in extreme cases, either extremely dense or sparse electron gas. ϵ_c in modern LDAs is expressed in parameterized formula, where the coefficients in the functional are fitted to accurate Quantum Monte Carlo calculations [24]. Different fitting formalisms of the ϵ_c lead to different LDAs, such as Perdew-Zunger [25], Perdew-Wang [26] *etc.*

The success of DFT is to a large extent due to the success of the initial applications of the LDA. Although the both the exchange and correlation parts of the LDA are known to contain significant errors compared to true many-body calculations, the overall results are quite accurate. This favourable error cancellation is due to the exchange-correlation hole satisfying the sum rule used in the LDA derivation [27, 28]. Due to the homogeneous gas assumption and the localized nature of the LDA, the LDA potential decays faster than the true V_{xc}. And it has tendency to offer stronger binding, upto 1 eV per bound.

Generalized Gradient Approximation

To improve over the homogeneous model used in LDA, the derivative of the charge density is included into the ϵ_{xc} functionals through $\nabla n(\mathbf{r})$.

$$\epsilon_{xc}[n] = \epsilon_{xc}[n(\mathbf{r}), \nabla n(\mathbf{r})]. \tag{2.31}$$

As suggested by Kohn and Sham [17], the Gradient Expansion Approximation (GEA) [29,30] was tried, but without success. The problem is that the charge gradient is too large to carry out a direct expansion. Generalized-Gradient Approximation (GGA) [31, 32, 32] modified the expansion to preserve the physical properties.

Based on different formalism [33, 34], the parameters in the modified expansion are fitted to either experimental data or other accurate non-empirical calculations. For example, the PBE [35, 36] functional is fitted to non-empirical data. The BLYP functional [37, 38] are fitted to experimental data from inert gas measurements. GGA usually is more reliable than LDA for the binding energy and quite reliable for most of the strong chemical bonds.

Both LDA and GGA have difficulties to capture strongly correlated electron states as in transition metal oxides, and also the dispersive van der Waals interaction. Improvement typically requires non-local or orbital-dependent E_{xc} functionals. For example, orbita-dependent formulations for strongly correlated electron systems called LDA+U [39, 40] has been quite useful, and the non-local functional DFT-vd2 functional has provided fairly good description of van der Waals interaction [41, 42].

2.3 Pseudopotentials

Kohn-Sham DFT makes many-body electron-electron calculation in real matters tractable. Electron-ion interaction is grouped into the external potential $V_{ext}(\mathbf{r})$. However, a naive implementation of the Coulomb potential of the nuclei is very expensive. There are several reasons for this [4]:

1 The electrical field is singular near the nuclei. Numerical treatment of a singular quantity is undesirable.

2 As the electronic states are orthogonal to each other, the wave functions near the nuclei have very rapid oscillations. It is costly to represent fast oscillations with a large number of Fourier components or a dense grid basis.

However, many of the properties of normal condensed matter have little to do with the tightly bonded core electrons or wave functions near the core region. Changes of the valence electron states are more responsive to environmental changes. In many physical circumstances, the nuclei and core electrons can be treated as a screened charged sphere. In fact, the electron-ion interaction is often quantified as a scattering phase shift, where the electron states outside the localized core region of a localized spherical potential can be derived analytically in terms of a phase shift. The goal of the pseudopotential is to replace the costly core-region valence wave functions with smooth ones, yet accurately represent the scattering phase shift outside the selected core region.

The first effective core-region potential, based on Orthogonalized Plane Waves (OPWs) formulism, is illustrated by Harring [43, 44] in 1940. The general idea of this formalism is described in exact valence and core states transformation by Pickett [45].

The valence electron states ϕ_v are orthogonal to all the core states ϕ_c, and thus have many wiggles near the core region. Both valence and core states satisfy

$$(\hat{H} - E_i)|\phi_i\rangle = 0,\ i = v, c. \tag{2.32}$$

A smoother pseudo valence orbital can be constructed by subtracting the core orbitals as

$$|\psi_v^{PS}\rangle = |\phi_v\rangle + \sum_c |\phi_c\rangle a_c, \tag{2.33}$$

Since $\langle\phi_c|\phi_v\rangle = 0$, $a_c = \langle\phi_c|\psi_v^{PS}\rangle$. Apply $\hat{H}$ to Eq. 2.33,

$$\hat{H}|\psi_v^{PS}\rangle = E_v|\psi_v^{PS}\rangle + \sum_c (E_c - E_v)|\phi_c\rangle a_c, \tag{2.34}$$

Rearrange the terms in Eq. 2.34

$$\left(\hat{H} + \sum_c (E_v - E_c)|\phi_c\rangle\langle\phi_c|\right)|\psi_v^{PS}\rangle = E_v|\psi_v^{PS}\rangle. \tag{2.35}$$

Eq. 2.35 is a generalized eigenvalue equation. The pseudo Hamiltonian $\hat{H}_v^{PS}$ for pseudo valence state $|\psi_v^{PS}\rangle$ is

$$\hat{H}_v^{PS} = \hat{H} + \sum_c (E_v - E_c)|\phi_c\rangle\langle\phi_c|. \tag{2.36}$$

With the $|\phi_c\rangle$ prepared as the effective atomic pseudo potential, the Kohn-Sham equation only solves for the pseudo valence state $|\psi_v^{PS}\rangle$.

The positive background provided by the nuclei becomes

$$\begin{aligned} \hat{V}_{ext}^{PS} &= \hat{V}_{ext}(\mathbf{r}) + \hat{V}_c \\ &= -\sum_I \frac{Z_I}{|\mathbf{r} - \mathbf{R}_I|} + \sum_c (E_v - E_c)|\phi_c\rangle\langle\phi_c| \end{aligned} \tag{2.37}$$

The screened ion core potential $\hat{V}_{ext}^{PS}$ is much weaker than the original $\hat{V}_{ext}(\mathbf{r})$. The $\hat{V}_{ext}(\mathbf{r})$ has a attractive (negative) contribution to the Hamiltonian, but the core electron contribution $\hat{V}_c$ is always positive (repulsive). $\hat{V}_{ext}^{PS}$ represents the effective potential felt by the valence electrons from the nucleus and core electrons.

To faithfully represent the screened nucleus core in different environments, norm preserving pseudo potential was proposed by Hamann *et al.* [46]. A norm preserving pseudo potential satisfies 4 desirable properties:

1 Pseudo valence states have the same eigenvalues as all-electron results at a chosen atomic reference configuration. The corresponding pseudo wave functions are the same as all-electron results at $r \geq R_c$, where R_c is a chosen "core radius".

2 The logarithmic derivatives of the pseudo valence wave functions agree with all-electron results for $r \geq R_c$ at energies around each E_v.

3 The integrals of charge densities from 0 to r, where $r \geq R_c$, for each pseudo valence states are the same as all-electron results.

4 The first energy derivatives of the logarithmic derivative of pseudo wave functions are the same as all-electron results at $r \geq R_c$.

The Point 1 is essentially saying the pseudo potential shall not change the valence state of the atomic reference configuration. It also ensures that the pseudo-potential outside the core region is the same as the all electron potential, since the eigenvalues and eigenstates are determined by the potential. Point 2 is a mathematical way of requiring that the pseudo potential does not change the energy-dependent scattering phase shift. When the value and slope of the logarithmic derivative of the pseudo wave function at $r \geq R_c$ is the same as that of the all-electron wave function, the scattering phase shift is uniquely determined. Point 3 makes sure that the total charge in the core region is correct and the normalized pseudo-orbital is the same as the true orbital at $r \geq R_c$. Points 2 and 3 ensure that the pseudo potential is transferable, which is required if a pseudo potential built under one condition can be used to accurately describe the valence states in different environments. Point 4 is to secure that in a different condensed matter environments, the changes in eigenvalues due to the change in the external surroundings can be reproduced accurately in a linear order.

Many different constructions have been used to satisfy those requirements. In a norm-conserving pseudo potential [46], the Point 4 is satisfied automatically by the Point 3. In an ultra-soft pseudo potential [47, 48], the Point 3 is relaxed by using an auxiliary overlap matrix. The Projector Augmented Waves (PAWs) [49, 50] method is a reformulation of the OPW that is satisfying the above requirements. It treats the localized functions near nuclei with muffin-tin methods. By a linear transformation, PAW relates the pseudo wave function with the all-electron wave function. Norm-conserving and ultra-soft pseudo potentials can be viewed as special cases under PAW [51].

2.4 Bloch Theorem and Supercell

Crystal structure is fully described by the ionic positions in one primitive unit cell and the set of translations that generate the periodic structure. The set of translations can be defined as

$$\{T_n\} = \{T_n : T_n = \sum_{i=1}^{d} n_i \mathbf{a}_i, n_i \in \mathcal{Z}\}, \tag{2.38}$$

with $\mathbf{a}_i$ being the the primitive translation vectors and d is the dimension of the space. The translation operator is defined as

$$\hat{T}_n \phi(\mathbf{r}) = \phi\left(\mathbf{r} + T_n\right) \tag{2.39}$$

It has the properties

$$\hat{T}_n \hat{T}_{n'} = \hat{T}_{n+n'} \tag{2.40}$$

The reciprocal lattice is defined with reciprocal primitive vector $\mathbf{b}_i$ as

$$\mathbf{G}_m = \sum_{i}^{d} m_i \mathbf{b}_i, \quad m_i \in \mathcal{Z}, \tag{2.41}$$

with

$$\mathbf{b}_i \cdot \mathbf{a}_i = 2\pi\delta_{ij}, \quad i = 1 \ldots d. \tag{2.42}$$

The periodic condition for the wave function requires the Born-Von Karman boundary conditions as

$$\phi(r + N_i \mathbf{a}_i) = \phi(\mathbf{r}), \quad i = 1 \ldots d, \tag{2.43}$$

or

$$e^{i\mathbf{k}\cdot N_i \mathbf{a_i}} = 1, \quad i = 1 \ldots d. \tag{2.44}$$

The reciprocal components for the wave function have the m_i index as

$$\mathbf{k} = \sum_{i}^{d} \frac{m_i}{N_i} \mathbf{b}_i, \quad m_i \in \mathcal{Z}, \tag{2.45}$$

N_i is the number of primitive cells along the direction labelled by the index i.

The physical quantities defined on the crystal structure are periodic. In both many-body and single-body system, the kinetic energy operator is invariant under any translation. In Kohn-Sham DFT, the effective non-interacting electrostatic potential $V_{eff}(\mathbf{r})$ has the same symmetry as the crystal lattice, thus it is also invariant under translations. Therefore, the Hamiltonian

of the crystal is translationally invariant and commutes with the translation operator,

$$\hat{H}\hat{T}_n = \hat{T}_n\hat{H}. \tag{2.46}$$

This suggests the eigenvalues and eigenstates of the $\hat{T}_n$ can be readily obtained through the relation in Eq. 2.40 and Eq. 2.45 as

$$\hat{T}_n\phi(\mathbf{r}) = t_n\phi(\mathbf{r}), \tag{2.47}$$

with

$$t_n = e^{i\mathbf{k}\cdot\mathbf{T_n}}, \tag{2.48}$$

$$\mathbf{k} = \sum_i^d \frac{n_i}{N_i}\mathbf{b}_i. \tag{2.49}$$

The eigenstate of $\hat{H}$ can also written as the right hand side of Eq. 2.47

$$\phi_k(\mathbf{r}) = e^{i\mathbf{k}\cdot\mathbf{r}}u_k(\mathbf{r}), \tag{2.50}$$

where $u_k(\mathbf{r})$ is a periodic function that $u_k(r + \mathbf{T_n}) = u_k(\mathbf{r})$.

Bloch theorem states that eigenstates of a translational operator $\hat{T}_n$ change by a phase factor in different periodic cells. It can apply to any translationally periodic function.

For non-periodic structures, *i.e.*, isolated molecules and surfaces, Bloch theorem can be used in combination with the supercell method. Supercell scheme constructs an artificial periodicity by including the non-periodic structures into one large simulation cell. The simulation cell is similar to the primitive unit cell originally used in the Bloch theorem. The non-periodic structures in the neighbor image cells are so far away from the structures in the simulations cell that they are essentially isolated in nature. For example, by including sufficiently large vacuum space in the simulation cell, a monomer molecule does not interact with its neighbour images. The properties of the molecule in this supercell are thus essentially the same as the isolated molecule.

2.5 Basis

2.5.1 Plane Wave Basis

The plane wave representation is the most widely used expansion in computational physics. The electron wave function in plane wave basis is

$$\phi_i(\mathbf{r}) = \sum_{\mathbf{k}} c_{i,\mathbf{k}} |\mathbf{k}\rangle, \tag{2.51}$$

with

$$|\mathbf{k}\rangle = \frac{1}{\sqrt{\Omega}} e^{i\mathbf{k}\cdot\mathbf{r}}, \tag{2.52}$$

$$\langle \mathbf{k}'|\mathbf{k}\rangle = \delta_{\mathbf{k},\mathbf{k}'}. \tag{2.53}$$

The Schrödinger equation becomes

$$\sum_{\mathbf{k}} \langle \mathbf{k}'|\hat{H}|\mathbf{k}\rangle c_{i,\mathbf{k}} = \varepsilon_i \, c_{i,\mathbf{k}}. \tag{2.54}$$

Since $V(\mathbf{r}) = \sum_m V_{\mathbf{G}_m} e^{i\mathbf{r}\cdot\mathbf{G}_m}$ and $\psi_k(\mathbf{r}) = \sum_m c_{i,\mathbf{k},m} e^{i\mathbf{r}\cdot(\mathbf{k}+\mathbf{G}_m)}$, the $\hat{H}$ in plane wave representation is

$$H_{m,m'} = \frac{\hbar^2}{2m_e} |\mathbf{k} + \mathbf{G}_m|^2 \delta_{m,m'} + V_{eff}(\mathbf{G}_m - \mathbf{G}_{m'}), \tag{2.55}$$

The plane wave basis is complete and converges well for soft pseudo-potentials, but since it is infinite, it must be truncated. A truncation criterion called cut-off energy E_{cut} is used to employ a finite size basis. It is defined in a kinetic energy expression as

$$E_{cut} \geq \frac{\hbar^2}{2m_e} |\mathbf{k} + \mathbf{G}_m|^2. \tag{2.56}$$

The error induced by basis truncation can be reduced to a negligible level in a practical usage by increasing the cut-off energy.

The speed of the plane wave Kohn-Sham DFT code is limited by the Fast Fourier Transformation (FFT) more moderate-size systems, and by diagonalization for large systems. The eigenstates are most efficiently solved in reciprocal space, but the charge density is most efficiently integrated over real space grid. The FFT is used to switch the functions between the reciprocal and real spaces. Its operational complexity is $O(n \log n)$, while diagonalization scales as $O(n^3)$ and dominates for large systems.

2.5.2 Real-Space Finite-Difference Method

Finite difference methods were developed for the Kohn-Sham DFT equation as an alternative to plane wave methods. Those methods are operate in real space [52]. In a grid-based real-space method, the operation of the effective potential on the wave functions is the direct summation of their products at each grid point. The laplacian in the kinetic operator can be calculated efficiently by high-order finite-differences. The performance is improved further by the short range nature of many quantities in the Kohn-Sham equation, whereas plane wave basis is essentially delocalized. Mathematically, the convergence can be systematically increased with a denser grid.

Chelikowsky *et al.* [53] expands the kinetic energy laplacian operator with central-finite-difference method on a real-space Cartesian grid with grid spacing h. At each direction at the grid point (x_i, y_j, z_k)

$$\left[\frac{\partial^2\phi}{\partial x^2}\right]_{(x_i,y_j,z_k)} = \sum_{-m}^{m} c_m \phi(x_i + mh, y_j, z_k) + O(h^{2m+2}). \tag{2.57}$$

c_m is the coefficient for the central-finite-difference.

A more efficient differentiation scheme was developed and implemented by Briggs *et al* [54, 55]. They used Mehrstellen operators to discretize the entire Kohn-Sham equation, not just the kinetic operator. Weighted sum of the wavefunctions and potentials is used to improve the overall accuracy. Moveover, Mehrstellen operators use grid points along all directions, rather than only those along Cartesian directions as in central-finite-method. This further improves the accuracy by using more local data. The discretized Kohn-Sham equation in a generalized eigenvalue form is

$$\mathbf{H}_{\text{mehr}}[\psi_i] = \frac{1}{2}\mathbf{A}_{\text{mehr}}[\psi_i] + \mathbf{B}_{\text{mehr}}[V_{eff}\psi_i]. \tag{2.58}$$

$\mathbf{A}_{\text{mehr}}$ and $\mathbf{B}_{\text{mehr}}$ are Mehrstellen discretization operators. Integrations are performed using the three-dimension trapezoidal rule

$$\int \mathrm{d}\mathbf{r} f(\mathbf{r}) \doteq h_{grid}^3 \sum_{ijk} f(\mathbf{r}(i,j,k)). \tag{2.59}$$

To get sufficient accuracy for electronic structure calculation, it is essential that the integrand $f(\mathbf{r})$ is band limited in the Fourier frequency range $G > G_{\max}$. High-frequency components could cause significant error in real-space integrations, even in a context of plane-wave calculations [56]. This effect can be best seen when the ions move relative to the grid points. The energy integrations with pseudopotentials in real-space can introduce unphysical variation. This variation were reproted as up 0.25 meV per atom [54].

The integration error can be reduced by explicitly eliminating the high-frequency part in calculations. In plane-wave calculations, high-frequency components are eliminated by the kinetic-energy cutoff. The "kinetic-energy cutoff" in grid-based real-space calculations is approximately $\pi^2/2h^2$, which is equal to that of a plane-wave based calculation using a FFT grid with the same spacing. However, unlike plane-wave calculations, frequency components larger than the kinetic-energy cutoff, $G > G_{\max} = \pi/h$, are nonetheless present on the grids. In practical real-space calculations, frequency components near or larger than $G_{\max}$ are Fourier filtered in pseudopotentials to reduce the integration error.

Above grid-based real-space methods usually generate a very large real, sparse $M \times M$ matrix, with M being the number of points on the real-space grid. Good iterative algorithm is very important to solve for the eigenvalues and wavefunctions. Briggs *et al.* used multigrid iteration techniques to accelerate residual reductions on a sequence of grids of varying grid spacing. The final solution is obtained on a sufficiently fine grid so that electronic wavefunctions and pseudopotentials are accurately represented. Successive auxiliary grids increasing spacing between grid points by a factor of two over the previous one are used to accelerate convergence at different length scales, *i.e.*, different Fourier frequency components. Iterations on any given grid levels are most efficient in reducing Fourier components of the error with wavelengths that are comparable to the grid spacing. By using multiple grids of varying resolutions, different frequency components of the error, upto the finest grid level, are efficiently reduced. The multigrid algorithm provides excellent preconditioning for multiple length scales and leads to rapid convergence rates. The operation count for one wavefunction scales as $O(N_{grid})$, compared to $O(N_{grid} \log N_{grid})$ for FFT-based algorithms in plane-wave calculations.

2.6 STM Simulation

STM images are calculated based on Tersoff's formalism [57]. For a small positive sample bias, the tunneling current density $j(\mathbf{r})$ is proportional to the local density of states (LDOS) at the tip position. With a simple extension of the expression derived by Tersoff and Hamann, the tunneling current density $j(\mathbf{r})$ could be expressed as

$$j(\mathbf{r}, V) \propto \int_{E_f - eV}^{E_f} \rho(\mathbf{r}, E)\, \mathrm{d}E, \tag{2.60}$$

where $\rho(\mathbf{r}, E)$ is the LDOS at the tip position, E_f the Fermi energy and V the tip bias. In my thesis work, most STM images are simulated to include the highest occupied electronic states (HOES). Depending on the size of different graphene configurations, different sample biases are used.

The simulated STM images crucially depend on the charge density of the sample surface.

STM images of most of the graphene flakes do not change patterns when the scan height ranges from 1 to 2 Å. In our constant-height STM image simulations, scan surfaces are chosen to be 1.5 Å above the graphene surface. The constant-current STM images are obtained by recording the isosurface of the surface charge density within the bias window.

Chapter 3

Edge and Vertex Effects on STM Patterns of Graphene Nanoribbons and Nanoflakes

Graphene is a promising material for nanoelectronics [58, 59]. At nanoscale, the effects of edges are important and must be understood. Using the real-space multi-grid method and density functional theory, we simulate STM images of nanoflakes and nanoribbons with different vertex types. Our results show that the edge type and vertex angle play an important role in determining the quasi-particle interference pattern. Various interference patterns, including (1x1) triangular, $\sqrt{3} \times \sqrt{3}$ R30° and hexagonal superstructures, can be generated with different vertices. Zigzag edge states are enhanced or reduced at the vertex corner, depending on the enclosed vertex angles. Armchair edges can have localized states due to bond length relaxation at edges.

3.1 Introduction

Understanding of graphene's intrinsic electronic properties, edge effects, and substrate influence is important for nanoscale applications. Scanning Tunneling Microscopy (STM) is often used to study the electronic states near graphene Fermi level. The measured state localization and electron interference patterns near edges and defects are the properties that characterize the electronic structure of the graphene edge.

For a free standing infinite graphene, Fermi surface collapses to six Dirac points near the boundary of Brillouin zone. In experimental conditions, graphene is usually slightly doped [60] and Fermi surface becomes circles centered on the respective Dirac cones. Wave functions near the Fermi energy have well-grouped wave vectors in six directions. At a low bias, an STM

experiment is imaging only a few of quasi-particle wave functions with a small set of wave vectors. Therefore, prominent charge density oscillations are expected [61].

In STM experiments, interferences at two length scales are expected with two categories of scattering vectors [62]. Short scattering vectors that are connecting k points on the same circle of the Fermi surface would lead to a long wave length charge density modulation in real-space. Long scattering vectors that connect k points on two circles centered on different Dirac points lead to interference patterns with a periodicity of $\sqrt{3} \times \sqrt{3}$ R30°. Interferences near defects on graphite surface and monolayer graphene are well-studied [62–65].

Graphene edges with various crystallographic orientations have been studied experimentally and theoretically [66–71]. Straight armchair edges on a graphite surface were identified as the source for honeycomb superstructure11 which consist of two sets of $\sqrt{3} \times \sqrt{3}$ R30° interferences. Zigzag edges do not show additional superstructures other than the graphite STM (1x1) triangular surface pattern (called 1x1 triangular pattern hereafter) [66, 68]. In areas far away from edges, (1x1) triangular surface pattern is recovered as on an infinite graphite surface, and graphene lattice is recovered on monolayer graphene [72]. Bernal stacking is believed to play a role in selecting one of the sublattices invisible on the graphite surface [73].

However, mechanically exfoliated graphene samples usually do not have very long straight edges. Many vertices are present that have well-defined angles restricted by the six-fold rotational symmetry of the graphene lattice. For a graphene sample with relatively smooth edges, vertices mostly have obtuse angles, such as 120° and 150°. The vertices are expected to influence the near-edge STM pattern. For instance, a mixture of zigzag and armchair edges was identified to introduce coexistence of the $\sqrt{3} \times \sqrt{3}$ R30° and the honeycomb superstructures in the experiment [70].

Graphene nanoflakes have more closely spaced vertices on edges. Lyding and Ritter [1] measured STM images on monolayer graphene nanoflakes, observing honeycomb superstructures in two graphene nanoflakes with very different edge types (Ref. [1] Figure 3bc). Interestingly, the patterns change depending on the shape of the flake and its edge terminations. However, since the nanoflakes are supported on silicon surfaces, substrate effects could also play a role, as could lattice defects. Furthermore, the experiments used current derivative imaging, which has not simulated up to now.

In this work, we investigate the vertex effects on edge states and STM patterns on graphene nanoflakes. STM and STM-derivative images are simulated with *ab inito* calculations using the real-space multi-grid method [55]. The source for observed experimental STM patterns is explained in our simulations. Our theoretical investigation shows that STM patterns depend critically on the interference of electron wavefunctions in different edge configurations.

3.2 Computational Methods and STM Simulations

The real-space multigrid method in the framework of density functional theory [54, 55] is used to calculate the electronic structures of nanoflakes and nanoribbons, employing ultrasoft pseudopotentials [47] and the Perdew-Burke-Ernzerhof exchange-correlation functional [35]. Twelve Angstroms vacuum regions in all directions are included in the supercell to ensure negligible interactions between periodic images. In simulations, the grid spacing is selected as 0.17 Å, which is equivalent to an energy cutoff of 47.8 Ry in a plane-wave representation. The structural relaxations are carried out until all the forces in the nanoflakes are smaller than 0.06 Hartrees/a.u.

The calculated C-C bond length for pristine graphene sheet is 1.42 Å. Bond length is 1.37 Å at the armchair edge and 1.41 Å at the zigzag edge. These results are in agreement with previous studies [74, 75].

STM images are calculated based on the Tersoff's formalism (see section 2.6) [57]. In order to compare directly with derivative STM images obtained in experiments, we also calculate the derivative STM current as

$$\hat{j}(\mathbf{r}, V) = \frac{\mathrm{d}j(\mathbf{r}, V)}{\mathrm{d}\hat{n}}, \tag{3.1}$$

where $\hat{n}$ stands for the fast scan direction in STM measurements.

3.3 Results and Discussion

Figure 3.1a shows a 1.73 nm wide armchair-edge graphene ribbon with one zigzag-edge vertex. Figure 3.1c shows a 1.79 nm wide zigzag-edge graphene ribbon with one armchair-edge vertex. In both cases, the angle between vertex edges is 120°.

In Figure 3.1b, honeycomb superstructure is shown in the middle of the graphene ribbon, indicated by a white hexagon. The HOES is the zigzag edge state, which is extended far beyond the vertex area. We will show in the next session that zigzag-edge nanoflakes with 120°-angle vertices can also make a similar STM pattern.

In Figure 3.1d, a rhombus-shaped low LDOS area appears near the armchair-edge vertex. The dark STM area shows all the carbon atoms, which are grouped into disconnected rings. It is a discontinuous zone for nearby zigzag edge states. Different from extended zigzag-edge vertex (STM pattern in Figure 3.1b), the characteristic low LDOS area is quite localized.

Note that the honeycomb superstructure in Figure 3.1b does not come from the 210° angle connections between the vertex and ribbon edges, because in Figure 3.1d, the honeycomb superstructure does not appear with the same connection configurations. The honeycomb superstructure is a property of the 120° zigzag vertex.

In our simulations, 210° angle vertices composed of different edge types do not show the

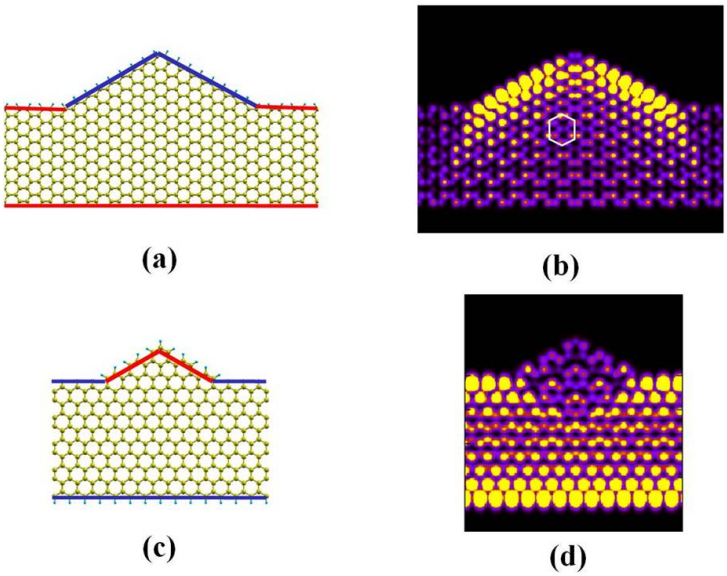

Figure 3.1: Atomic structures and STM images of graphene nanoribbons with a single vertex. (a) Atomic structure and (b) STM image of an armchair-edge GRN with zigzag edge vertex. (c) Atomic structure and (d) STM image of a zigzag-edge GRN with armchair edge vertex. The crystallographic orientations of graphene edges are labeled as armchair (red) and zigzag (blue).

simultaneous $\sqrt{3} \times \sqrt{3}$ R30° and honeycomb patterns. This is different from the results of 270° and 300° angle vertices [68]. The $\sqrt{3} \times \sqrt{3}$ R30° and honeycomb patterns thus have dependencies not only on edge types, but also on vertex angles. Furthermore, in graphene samples with a mixture of zigzag and armchair edges, the quasi-particle interference pattern is always dominated by the edge states near the Fermi level. The interference patterns, if any, of nearby armchair edges will not be clearly visible in experiments.

Two hexagonal graphene nanoflakes of about 2 nm side lengths were shown in experimental topological derivative STM images (Ref. [1] Figure 3bc). Each one was dominated by one crystallographic edge type. Four edges were identified and labeled in the experiment. The honeycomb superperiodic pattern was seen in both samples.

We study equilateral hexagon with 19.8 Å zigzag edges (Figure 3.2a) which is similar in size and shape to the experimental sample shown in Ref. [1] Figure 3b. Strong edge states from the six zigzag edges dominate and show a (1x1) triangle pattern in the simulated STM image, in contrast to the observed honeycomb superstructure. However, the equilateral hexagon has six zigzag edges instead of four in the experimental sample.

To avoid speculations about the two not-identified edges in experimental observations and to isolate the influence of these four zigzag edges, we calculated images of an elongated hexagon (Figure 3.2d). The elongated hexagon has four short zigzag edges 19.8 Å long and two 59.4

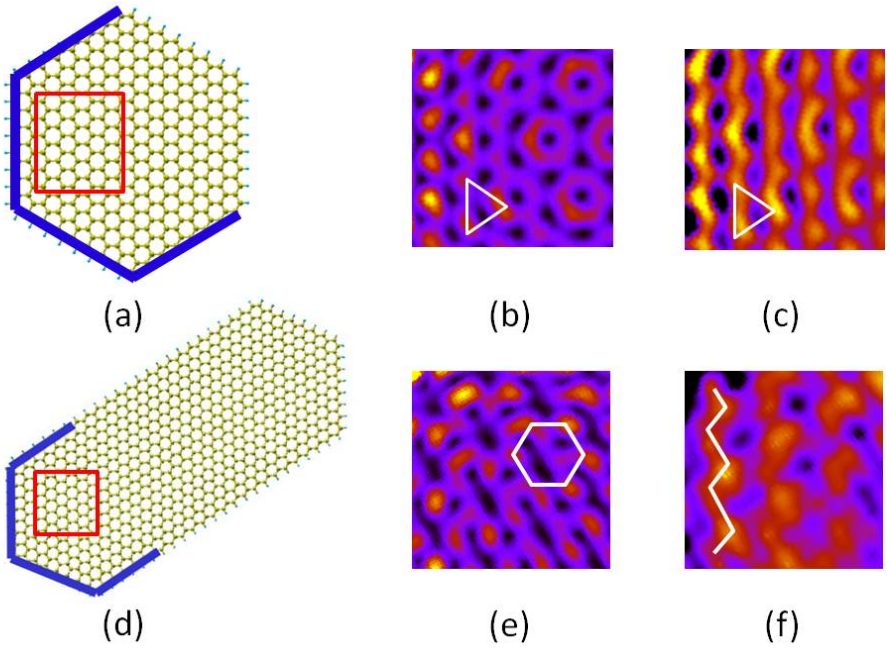

Figure 3.2: Simulated STM images for zigzag-edge graphene nanoflakes. (a) Atomic structure of an equilateral hexagonal flake. (b) Derivative STM image and (c) Normal STM image for the area indicated by the red square in (1). (d) Atomic structure of an elongated hexagonal graphene flake. (e) Derivative STM image and (f) Regular STM image. The directional derivative (fast scan) directions is horizontal.

Å edges. A weak honeycomb pattern occurs in the simulated STM image near the 120° vertices, which is in relatively similar position as in Figure 3.1b. After the topological derivative along the fast scan direction is taken, the simulated STM image of the elongated hexagon gives a comparable zigzag chain pattern (Figure 3.2f) to the experimental observation. These three consecutive 120° zigzag vertices lead to the honeycomb superstructure observed in experiment.

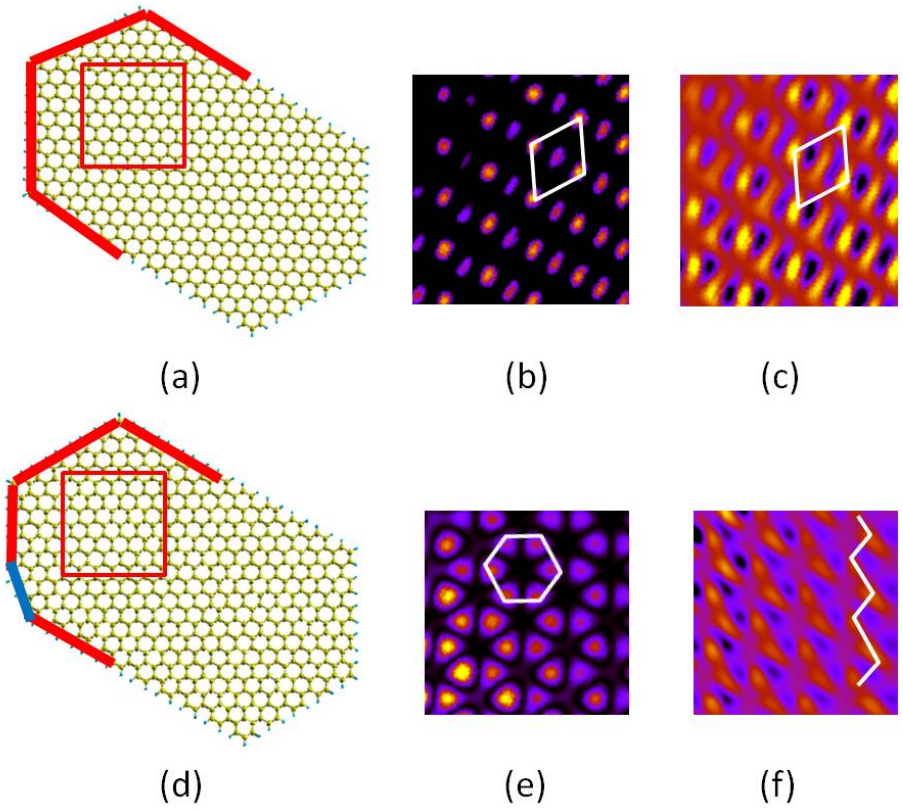

Figure 3.3: Simulated STM images for armchair edge-dominated samples. (a) Atomic structure of an elongated hexagon with armchair edges. (b) Normal and (c) Derivative STM images of the area indicated by red square in (a). (d) Atomic structure of an elongated hexagon with mixed armchair and zigzag edges. (e) Normal and (f) Derivative STM images of the area indicated by red square in (d). The red lines are armchair edges and the blue line is a zigzag edge.

To study the armchair-edge graphene sample observed in the experiment (Ref. [1] Figure 3c) an elongated hexagon graphene flake is simulated with one end having the same edge shape (Figure 3.3d). One short zigzag segment is introduced at one of the joints to simulate the experimental situation. The length of the edge segments is set close to the experimental

sample. A strong honeycomb superstructure is observed (Figure 3.3e) in the area corresponding to the experimental sample and the derivative image (Figure 3.3f) agrees with the experimental results.

Interestingly, when the zigzag segment is eliminated, the honeycomb pattern disappears. An elongated armchair hexagonal graphene flake with the same geometrical shape is calculated, except that the short zigzag corner is replaced by a well-defined pure armchair-edge vertex (Figure 3.3bc). The normal STM image shows a clear $\sqrt{3} \times \sqrt{3}$ R30° pattern, but not the honeycomb pattern. The derivative STM image also differs from the experimental image substantially. The 150° vertices jointing the zigzag and armchair edges turn out to be the source of the honeycomb superstructure observed in the experiment.

3.4 Edge States at Different Vertices

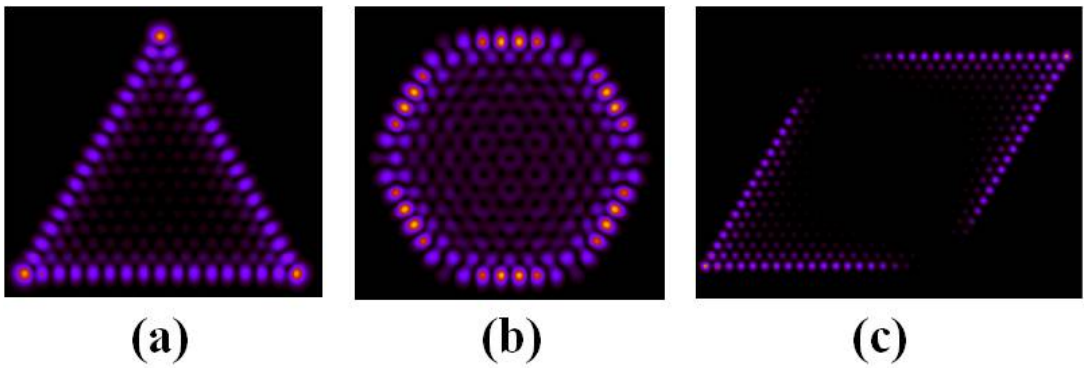

Figure 3.4: Simulated STM images for edge state of zigzag-edge graphene nanoflakes. (a) Equilateral triangle graphene nanoflake with 60° vertices. The side length is 3.91 nm. (b) Equilateral hexagonal nanoflake with 120° vertices. The side length is 1.98 nm. (c) Equilateral rhombus nanoflake with 60° and 120° vertices. The side length is 4.95 nm.

Figure 3.4 shows three graphene nanoflakes with zigzag edges: an equilateral triangle, an equilateral hexagon, and an equilateral rhombus. Zigzag edge states are enhanced on corners of 60° vertices, but reduced on those of 120° vertices. In the equilateral rhombus graphene nanoflake with edge length of ∼5 nm, LDOS difference between 120° vertices and 60° ones is clearer.

One of the most important differences between 60° and 120° vertices is that edges in 60° vertices are from the same sublattice, while those of 120° vertices are not. The LDOS is enhanced at corners composed of the same sublattice, but is reduced at corners composed of

different ones.

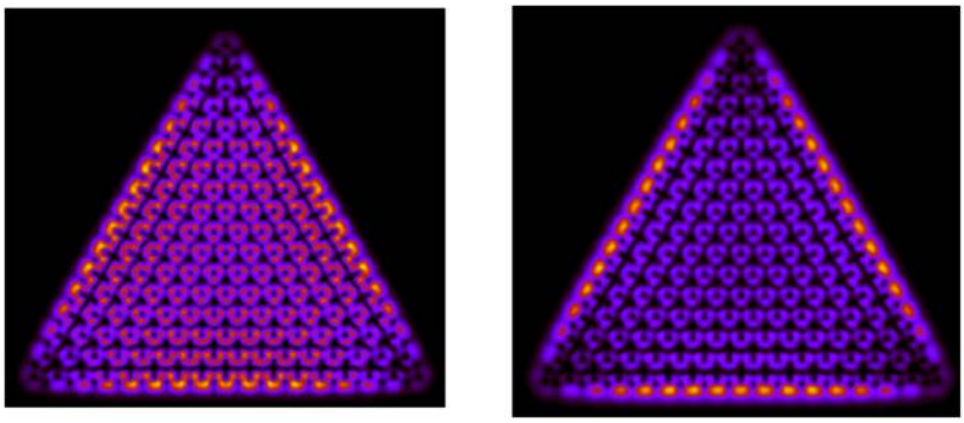

Figure 3.5: Simulated STM images of the HOMO state of an equilateral triangle nanoflake with armchair edges. STM scan heights are (a) 1.3 Å and (b) 3.3 Å above the graphene sample.

Different from the zigzag graphene edge, an armchair edge does not induce strong localized state at the Fermi level. However, our simulation shows that an STM experiment may still observe an "edge state" for a pure armchair-edge graphene flakes. Figure 3.5 shows simulated STM images of an equilateral triangle nanoflake with armchair edges. Our simulated STM images can change with different tip-sample distances, *i.e.*, STM scan heights in experiments. When the scan plane is 1.3 Å above the graphene flakes, the HOES appears to be an extended state, with a brighter area near the armchair edge. The charge density shows the graphene lattice, yet respecting the flake's symmetry (Figure 3.5a). When the scan plane is increased to 3.3 Å above the graphene flake, the HOES is clearly localized at the edges.

This distance effect armchair edges essentially has the same mechanism as the distance-dependent STM images of graphite defects7. After atomic relaxation, armchair-edge graphene flake has different bond lengths at the center than at the edges [74, 75]. The bond length at the relaxed armchair edge is 1.37 Å, shorter than the 1.42 Å C-C bond length in the center area. Bond length changes near the armchair flake edges could be taken as a perturbation to an imaginary 1.42 Å armchair edge.

3.5 Summary

In the frame work of density functional theory, we used real-space multigrid method to investigate graphene interference patterns near edge vertices, which can help to understand the factors influencing STM images.

Edge types and vertex angles determine the quasi-particle interference patterns in graphene samples. The 120° zigzag edge vertex creates the honeycomb superstructure, which extends far beyond the vertex area. At low bias, the 120° armchair-edge vertex alters only a small LDOS area at nearby zigzag edge states, and does not creat a clear interference pattern.

STM images of graphene flakes are very sensitive to the edge configuration. We reproduced the experimental STM observations and identified the sources of the observed STM patterns. 120° zigzag vertices in zigzag-dominated graphene nanoflakes and 150° armchair-zigzag vertices in the armchair-dominated graphene flakes are the sources of honeycomb superstructure in the respective experimental samples.

For zigzag-edge vertices, edge states are enhanced at 60° vertex corners, but are reduced at 120° ones. This is due to the fact that edge atoms at 60° vertices belong to a single sublattice, while in 120° zigzag vertices the atoms at the two edges belong to different sublattices. For an armchair-edge vertex, a scan-height-dependent "edge state" is predicted. Furthermore, LDOS near an armchair edge decays slower than that in the center of the nanoflake. This is introduced by the perturbation potential due to shorter bond lengths at armchair edges.

Chapter 4

Supramolecular Self-Assembly of π-conjugated Hydrocarbons *via* 2D Cooperative CH/π Interaction

Supramolecular self-assembly on well-defined surfaces provides access to a multitude of nanoscale architectures, including clusters of distinct symmetry and size. The underlying driving forces that lead to such self-assembled supramolecular structures generally involve both graphoepitaxy and weak directional nonconvalent interactions. Here we show that functionalizing a benzene molecule with ethyne group introduces attractive interactions in a 2D geometry, enabling supramolecular self-assembly in a system that would otherwise be dominated by intermolecular repulsion. Furthermore, a subtle balance between very weak CH/π bonding and molecule-surface interactions produces a well-defined "magic" dimension and chirality of supramolecular clusters. The nature of the process is corroborated by extensive scanning tunneling microscopy/spectroscopy (STM/S) measurements and *ab initio* calculations, which emphasizes the cooperative, multi-center characters of the CH/π interaction. This work points out new possibilities for chemical functionalization of π-conjugated hydrocarbon molecules that may allow the rational design of supramolecular clusters with the desired shape and size.

My role in this study was to perform the theoretical analysis and calculation in this joint experimental and theoretical work. Most of this chapter has been published in ACS Nano 6, 566-572 (2012) [76].

4.1 Introduction

One of the outstanding paradigms of nanoscience [77] is that of "magic" nanoparticles or molecular assemblies. For example, single atoms aggregate into a cluster with well-defined shape and

size due to favorable saturation of the electronic shell in a particular "magic" atomic configuration [78]. Likewise, organic molecules can be self-assembled into magic clusters if there exists a structure that saturates the coordination shells of the constituent molecules bonded *via* specific interactions [79–81]. Weak directional molecular forces hence are central to self-assembly in general, and are particularly important for the formation of supramolecular structures on surfaces because they provide a balance between intermolecular and molecule-surface interactions, as well as the feasibility of coordination shell saturation.

Of the candidate attractive interactions, the hydrogen bonding is by far the most significant. Typically, supra- and extended molecular structures are produced by functionalizing such molecules with strongly polar groups (such as OH, COOH, NO_2 *etc.*), and the ensuing hydrogen bonding (enthalpy varying from 3 to 7 kcal/mol) [82, 83]. However, electrons in C-C π-bonds, particularly those of the triple bond, can also act as a soft base and form the so-called XH/π hydrogen bond (X=O, N and halogen) with a comparatively smaller enthalpy, i.e. from 2 to 4 kcal/mol [84]. In some special cases, the carbon atom itself can act as a soft acid leading to CH/π hydrogen bonds [85, 86] , with an enthalpy varying from 0.5 to 2 kcal/mol (the weakest of the hydrogen bonds). The potential advantage of CH/π bonding is its directionality (the CH fragment points perpendicular to the π orbital in a single CH/π bond) and the highly cooperative nature due to the ability of the CH/π fragments to act as both a Lewis acid and base.

Here I discuss a combined theoretical and experimental study that explores the possibility of utilizing weak CH/π bonding to enable 2D supramolecular self-assembly of flat-lying π-conjugated molecules. The latter, for examplebenzene and pentacene, have long been a basic model system for an organic-metal interface that is key to a variety of electronic and energy-related applications. CH/π bonding between aromatic molecules on surfaces has been implicated previously, but so far primarily in 3D molecular assemblies [87, 88] , where phenyl rings can orient normal or close to normal to each other. A parallel relative orientation of the π-conjugated system in the 2D geometries results in repulsive intermolecular interactions, preventing significant ordering within the molecular layer up to a relatively high coverage [89, 90]. We will show that involving ethyne groups as a source of attractive intermolecular interactions can solve this problem and enable supramolecular self-assembly in a 2D geometry.

4.2 Methods

Sample preparation and STM measurements were performed in an ultrahigh vacuum system (base pressure is better than 1×10^{-10} mbarr). Experiments were conducted with a home-built variable temperature scanning tunneling microscopy (VT-STM), whose temperature can vary from 25 K to 300 K. In the present investigation, if not otherwise mentioned, all the STM/S

measurements are performed at 28 K. Phenylacetylene molecules were purified by the standard freeze-pump-thaw process. The Au(111) surface was cleaned by standard Argon sputtering-annealing cycles before deposition of phenylacetylene molecules. The Au(111) substrate is kept at 50 K during the molecular deposition. A commercial Pt-Ir tip was carefully prepared by gentle field emission with clean Au(111) sample. The STM images were analyzed using WsXM [91].

To compute the STM image, we first use PBE and vdW-DF to relax a hexamer on Au(111). We placed the hexamer structure on top of the Au surface in a position such that the center of each phenyl's ring was placed approximately above one of the Au atoms of the first layer. Two layers of Au were used to represent the Au(111) surface. The hexamer/Au(111) system was relaxed by keeping the Au atoms frozen and letting the hexamer relax fully. The calculations were done with the PWscf software [92] and took into account dipole corrections [93]. An energy cutoff of 544 eV, and a $2 \times 2 \times 1$ k-point mesh with a Gaussian smearing of 0.02 eV were used. The relaxation was carried out until the forces in the hexamer were smaller than 0.001 Ry/a.u.

The NBO analysis was performed with the NWChem software [94] and employing PBE with the DFT-D2 approach.

Relaxation of the clusters in gas-phase was performed using PBE and vdW-DF in a unit cell of dimensions $40\,\text{Å} \times 40\,\text{Å} \times 28.5\,\text{Å}$, which is large enough to avoid interaction between periodic images. The clusters were relaxed only in 2 dimensions, except for the 7' cluster, in which one phenylacetylene (the one in the plane perpendicular to that occupied by the hexamer) was allowed to relax in every direction.

The PDOS of the hexamer in gas-phase and on Au(111) was computed by PBE and vdW-DF.

4.3 Results and Discussion

After low temperature deposition of ∼0.1 ML, the phenylacetylene molecules (Figure 4.1a) cluster into largely disordered structures within the fcc domains of the Au(111) surface (Figure 4.1b). The height of a single molecular layer is around 0.15 nm, typical for flat-lying π-conjugated molecules [89, 95]. Supramolecular self-assembly of regular clusters is triggered by post-annealing the sample to ∼120 K for 10 minutes, wherein most of the molecules on the surface rearranged into a single type of cluster with regular triangular shape and exactly six constituent phenylacetylene molecules, which we refer to as a hexamer in the following. Increasing the coverage up to 0.3 ML only produced more hexamers, but neither their shape nor their internal structure changed (Figure 4.1c). The highly preferential formation of hexamers, in a broad range of surface coverage (see appendix A, Figure A.1) signifies the existence of "magic"

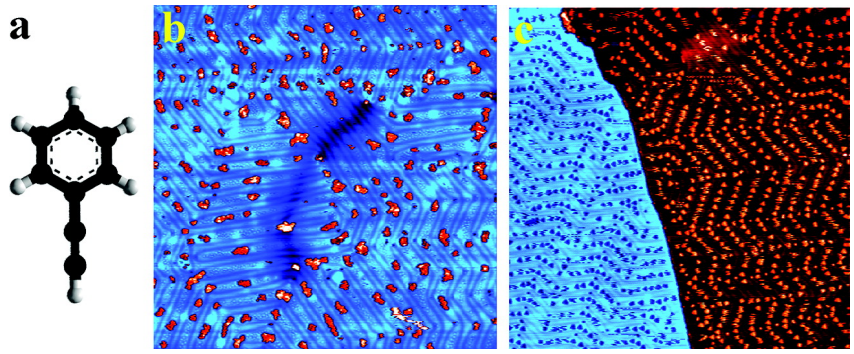

Figure 4.1: Topographic STM images of phenylacetylene molecules on Au(111), as-grown and after postannealing: (a) molecular structure of phenylacetylene; (b) phenylacetylene molecules form clusters after low temperature deposition at 50 K (800 mV, 30 pA), image size = 130×130 nm^2; (c) molecules self-assembled to form magic clusters array after annealing at 120 K (1 V, 30 pA), images size = 160×160 nm^2.

rules that underpin supramolecular self-assembly of phenylacetylene on Au(111) (see appendix A, Figure A.2, A.3).

Within the hexamer, one can differentiate three edge molecules forming a pinwheel arrangement with $\sim$120° relative angle between molecular axes, and three corner molecules each at $\sim$90° angle with respect to its edge neighbor (Figure 4.2a). The central pinwheel has a three-fold symmetry axis but no mirror planes perpendicular to the surface, which gives rise to chirality. We schematically label this chirality as either a clockwise (C) or anticlockwise (A) orientation of the hexamer (see Figure 4.2a). From inspection of a large number of hexamers, we established that all A (and C) hexamers are oriented exactly the same way with respect to the surface, or equivalently. Each complex can rotate only by 120°, and no other angle. If we assume that the all phenylacetylene molecules within the hexamer occupy approximately the same surface site, it is straightforward to verify that there exists only one way to arrange the hexamer over the Au(111) surface that would satisfy the observed chirality, three-fold axis of rotation and the relative $\pm$9° angle between the "axis" of the hexamer and the $\langle 11\overline{2} \rangle$ direction of the Au surface (Figure 4.2b and 4.2c). The corresponding structure is schematically shown in Figure 4.2a, where all the phenyl rings of the constituent molecules positioned over the fcc-hollow sites and the hexamer became centered approximately around an on-top surface site.

The involvement of CH/π bond in the stabilization of the hexamer is evident from the relative orientation of the ethyne groups, specifically the 90° angles between each corner molecule and its central neighbor, anticipated for CH/π bonding [85]. The structure of the hexamer also suggested that the phenyl ring did not contribute in the CH/π bonds. This is due to the

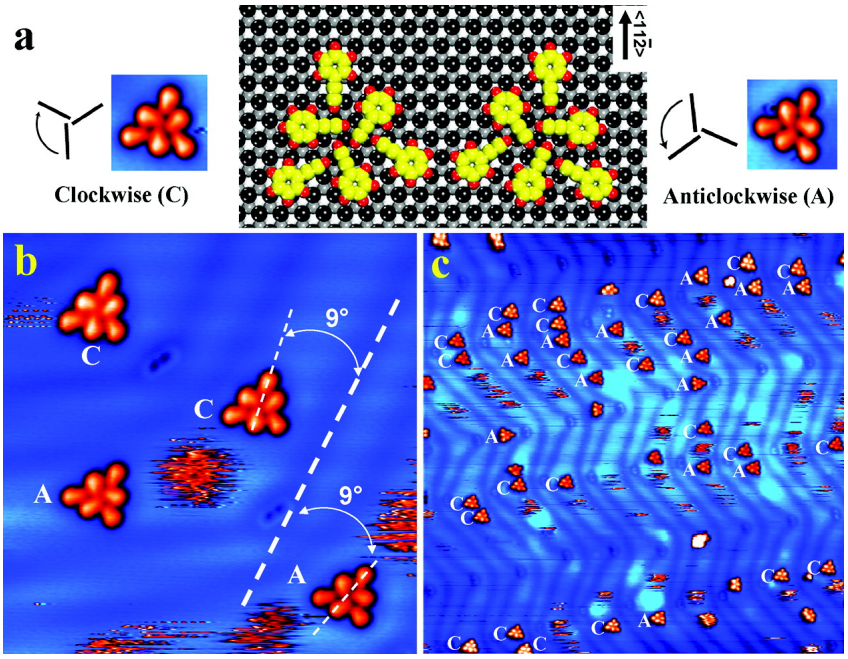

Figure 4.2: Chirality of the hexamer: (a) structural models showing the inferred adsorption configuration of hexamers with clockwise (C) and anticlockwise (A) chirality, mirrored with respect to $\langle 11\bar{2}\rangle$ direction of the Au(111) substrate. Enlarged STM images show the individual hexamer. (b) High resolution STM image showing few hexamers with both C and A chiralities (600 mV, 50 pA). White dashed line indicates the soliton line ($\langle 11\bar{2}\rangle$ crystallographic direction). Image size: 20×20 nm^2. (c) More hexamers in a larger area scan (800 mV, 30 pA), 60×60 nm^2.

surface parallel orientation of the π-conjugated phenyl ring, which prevents CH/π attractive interactions between the flat-lying phenyls. Notably, the relative angles between edge molecules in the pinwheel are 120°.

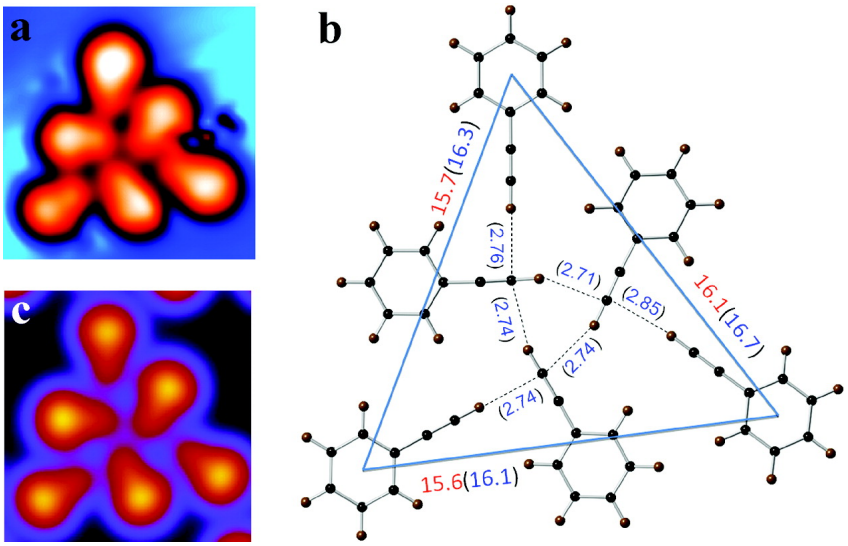

Figure 4.3: High-resolution STM image of a hexamer as well as its calculated structure. (a) High resolution STM image showing the internal structure of hexamer. (b) Structural model for the hexamer. Distances between the center of the rings of individual corner phenylacetylene molecules and the bonding lengths for each CH/π bonds are presented, in which experimental data are highlighted by red and calculated values are shown as blue numbers in brackets. (c) Theoretical simulated STM image for the fully relaxed hexamer on two layers of Au(111).

To gain further insight into the hexamer's structure and bonding mechanism, a hexamer was placed on a slab of Au(111) and relaxed using Density Functional Theory (DFT) calculations, with the PBE [35] functional and long-range interactions accounted for by the van der Waals (vdW)-DF approach [41]. The relaxed structure of the hexamer on Au(111) is shown in Figure 4.3b, and it is in very good agreement with the experimental observation: its size (the average distance between the centers of two corner molecules) is 16.4 Å, very close to the experimental value of 15.8 ± 0.5 Å; the average length of the CH/π bonds in the relaxed hexamer is 2.76 Å, in the upper range of bond lengths known from bulk experiments [96] ; and the simulated STM image (Figure 4.3c) with sample bias of 800 meV agrees well with the experiment (Figure 4.3a).

The underlying bonding mechanism was investigated by performing a Natural Bond Orbital (NBO) [97] analysis for the relaxed structure of the hexamer. NBO analysis not only confirms

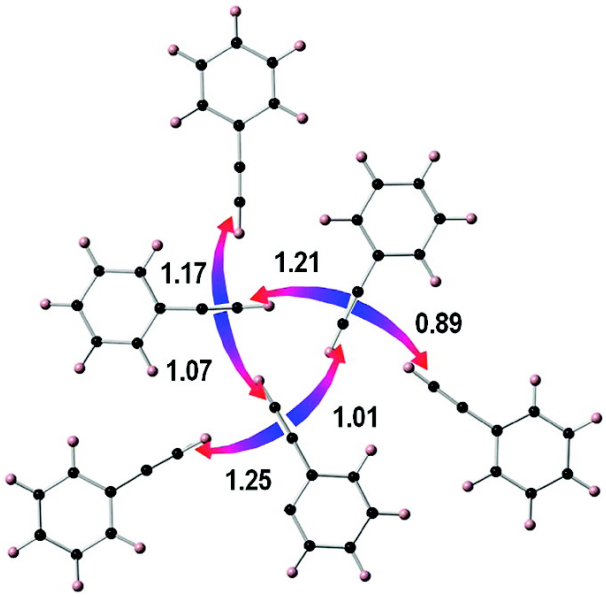

Figure 4.4: NBO analysis of the bonding motif for the relaxed hexamer. The arrows indicate the direction of electron transfer and the numbers above each arrow stand for the computed stabilization energy (in kcal/mol). The colors of each arrow indicate electron donor (blue) or electron acceptor (red) behavior.

the CH/π bonding, but also clearly emphasizes its cooperativeness (Figure 4.4): each edge molecule acts as an electron acceptor for one of its edge neighbors, and as an electron donor for one edge and one corner neighbor. On the other hand, each corner molecule is only an electron acceptor from one of the edge phenylacetylene molecules. In every case, the stabilization energy varies between 0.9 and 1.2 kcal/mol within the energy window of CH/π bonds (0.5–2 kcal/mol).

There remains a question of why six molecules is the "magic" number on Au(111). To address this question, we have computed the binding energies of gas-phase clusters comprised of two, three, four, five, six, seven, and eight phenylacetylene molecules using PBE and vdW-DF (see Figure A.5a). The binding energies are defined here as the energy gained by forming a cluster from isolated phenylacetylene molecules. We did not find a pronounced energy minimum for a hexamer (see Figure A.5b) and thus infer that Au(111) substrate must play a crucial role in stabilizing the hexamer.

For starters, the hexamers are mostly located at the fcc domain of the herringbone structure of Au(111). A similar phenomenon has been reported for many other molecules [98, 99] on Au(111), and it can be understood on the basis of the domain dependence of the electronic potential [100] or, alternatively, the anisotropy of the adsorbate-induced stress [101]. However, we observed significant adsorption of both disordered and supramolecular clusters only within the fcc-region. Thus, we believe that the preference toward the fcc-stacked region cannot explain

the stability of the hexamer.

A more relevant property is the epitaxial relationship of the hexamer relative to the surface (Figure 4.2a), which has been inferred above from the statistics and relative orientation of the chiral supramolecular clusters. To probe the preferred adsorption site of the hexamer on the Au(111) surface, we have used *ab initio* techniques to calculate the binding energy of the hexamer in six different configurations, denoted here as fcc, top, hcp, bridge-hcp-fcc, bridge-hcp-top, and bridge-top-hcp (see Figure A.6a in appendix A for details). The binding energies were computed employing the Density Functional Theory (DFT) with the PBE approximation to the exchange correlation potential, and the DFT-D2 approach of Grimme [102] to account for weak dispersion interactions. The results are shown in Figure A.6b of the appendix A. The fcc adsorption site is most stable, followed by hcp at about 47 meV apart. These results support the observation that there exists an epitaxial relationship between the molecules within the hexamer and the underlying lattice.

What happens if a seventh molecule is added to the hexamer in the 2D geometry? Maintaining a flat overall structure would make it necessary for the angle between this corner molecule and its bonded edge partner to deviate from 90°, in line with the 120° angle formed by cooperative CH/π bonding within the pinwheel center of the hexamer. Steric repulsion would clearly not favor this scenario, necessitating significant disruption of the central-corner bonding, and by extension of the other bonds within the hexamer. Furthermore, the seventh molecule would not be able to occupy the same surface site as its neighbors, still avoid significant steric repulsion, and optimize the CH/π bonding. Therefore, the hexamer is most likely the lowest-energy arrangement that satisfies three criteria: (1) maximum overall saturation of the coordination shell of the cooperative CH/π bond; (2) 2D geometry; and (3) favorable adsorption site for all the constituent molecules. Although we do not have the final answer for the origin of the "magic" rule at present, our findings immediately suggest that one should be able to form different supramolecular "magic" clusters by using different substrates.

The electronic properties of the hexamer were investigated by measuring the distance–voltage (Z–V) spectra [103, 104], which register displacement of the tip relative to the surface with increasing bias. When a resonance, such as a molecular state, falls into a tunneling window, an abrupt increase of the tunneling conductance takes place, which results in a step-like feature in the z-displacement (see Figure A.4). The numerically differentiated ($\mathrm{d}Z/\mathrm{d}V$) spectra acquired over a corner or central molecules are shown in Figure 4.5a. When the tip is placed over a corner molecule, a peak centered at ∼3.32 V is registered, whereas a peak centered at ∼3.21 V appears when the tip is placed over a central molecule. We argue that these peaks are associated with the collective lowest unoccupied molecular orbital (LUMO) state of the hexamer.

We computed the Projected Density of States (PDOS) of the hexamer placed on Au(111)

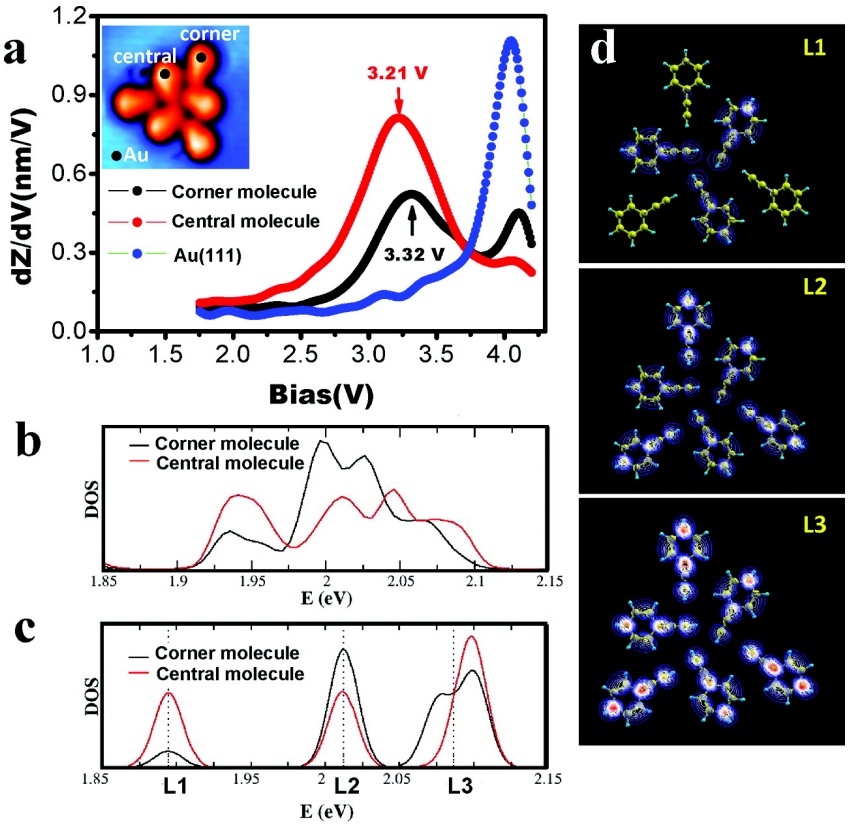

Figure 4.5: Electronic properties of a hexamer. (a) Numerically differentiated distance–voltage signal against the applied sample bias, $\mathrm{d}Z/\mathrm{d}V$, showing the LUMO states of the corner and central molecule in the hexamer. Inset figure shows locations of distance–voltage (Z–V) spectroscopic measurements over a corner, central molecule and bare Au surface, respectively. (b and c): *Ab-initio* projected density of states (PDOS) for the corner and central molecule sites in the hexamer on Au(111) and in the gas phase hexamer, respectively. The peaks L1, L2, and L3 in panel c correspond to the first six LUMO states of the hexamer. (d) Wave functions' moduli of the three peaks labeled in panel c.

surface by taking the sum of the PDOS for the phenyl rings of corner and edge molecules (Figure 4.5b). Two peaks are observed and both have contributions from the corner and edge molecules. This already implies that the LUMOs of the parent molecules sufficiently hybridize and form several states split in energy. The peak below 2 eV has larger weight on the central molecule, while the higher-energy peak has a majority component on a corner molecule. The calculated splitting is thus in qualitative agreement with the measured trend. The overlap of the constituent LUMO states is most clearly observed in the gas-phase PDOS calculations (Figure 4.5c and 4.5d), where three distinct energy levels are formed as a result of the overlap of LUMOs of the individual moleculars.

4.4 Conclusion

We successfully synthesized uniform hexamers made of phenylacetylene molecules on the Au(111) surface. Both experiment and theory suggest that a balance between CH/π and surface-molecule interactions drives the favorable formation of the hexamers. Both the directionality and multi-centricity of the CH/π bond appear to be critical for supramolecular self-assembly, dictating the number of molecules within the assembly and their relative orientation. It also appears that the substrate may play a significant role in defining the "magic" number six. Finally, Z–V spectroscopy has further revealed that the electronic properties of the molecules are modified upon self-assembly, specifically causing significant overlap of the LUMO states despite of the relatively weak intermolecular interactions. We envision that adding more acetylene groups to the phenyl ring or using different substrates will allow for additional structural flexibility and possibly tunable control over the shape and the size of supramolecular assemblies, as well as the transition between supramolecular and extended self-assembled structures.

Chapter 5

Electronic Control over Attachment and Self-Assembly of Alkyne Groups on Gold

Self-assembled monolayers are the basis for molecular nanodevices, flexible surface functionalization and dip-pen nanolithography. Yet self-assembled monolayers are typically created by a rather inefficient process involving thermally driven tethering reactions of precursor molecules to a metal surface, followed by a slow and defect-prone molecular reorganization. Here we demonstrate a non-thermal control over the self-assembly of phenylacetylene on gold that produces previously unachievable well-ordered three-dimensional monolayers, where the molecules are attached directly through the alkyne group. While thermal excitation can only desorb the parent molecule due to prohibitively high activation barriers for attachment, localized injection of hot electrons or holes not only overcomes this problem, but also enables an unprecedented control over subsequent ordering of attached molecules on the surface, including a nanoscale control over the size and shape of the self-assembly, defect structures and the reversible process between flat-lying and upright molecular configurations from single molecular level to mesoscopic scale. This work thus demonstrates the feasibility of non-thermal reaction pathways that may lead to unique and controllable self-assembly in supported molecular layers.

My role in this research was to perform theoretical analysis and calculations for this joint experimental and theoretical project. Most of this chapter has been published in ACS Nano 6, 9267-9275 (2012) [105].

5.1 Introduction

Alkanethiol self-assembly on gold has produced thousands of new applications involving surface functionalization, paved ways to new research areas, such as molecular electronics [106,107] and enabled dip-pen nanolithography [108]. Much of the success of this particular system is rooted in the 3D character of the alkanethiol self-assembled monolayers (SAM)s, where the molecular tails are decoupled from the metal support, form dense packing and enable subsequent attachment of complex functional molecules to surfaces [109,110]. The properties of the sulfur-anchor group of the alkanethiol molecule are evidently critical for the transition to a 3D geometry, though many of the details of the latter are still unknown [111]. Yet the necessity to search for an alternative is motivated by the overall complexity of the sulfur-gold chemistry, which among other things produces numerous defects within the monolayer [110–114]. Furthermore, on a fundamental level, relying on thermal fluctuations to drive the tethering reactions reduces the degree of control over the interfacial chemistry, and necessitates non-trivial approaches [115,116] to nanoscale patterning or substitution reactions within the self-assembled layer.

An intriguing alternative anchor is the alkyne group [117–121]. Based on the early theoretical analysis [117], the alkyne group can form several stable bonding derivatives on the prototypical Au(111) surface. Furthermore, some of the derivatives can maintain π-conjugation down to the gold surface [121], which may be beneficial for electron transport across metal-organic interfaces. However, theoretical calculations suggested that the stability of the alkyne bond itself gives rise to a very high activation barrier for the tethering reaction and largely precludes a thermally-activated reaction [117]. To make SAMs with alkyne groups, experiments have therefore focused on the oxidation of the alkyne group [121, 122], but a clear ordered arrangement has so far been elusive, and the requirement for an oxidant significantly complicates the methodology for the self-assembly and the chemistry involved.

Here we demonstrate that electron-induced reactions of the alkyne group overcome the challenge of the prohibitively high activation barrier, and produce a well-ordered self-assembled monolayer by switching the molecular orientation from flat-lying to upright. Moreover, the electron-induced reactions is completely controllable and reversible, with an unprecedented control over the position, size, shape and defect structures of molecular assemblies from single molecular level to mesoscopic scale. Hot-electron reactions may therefore become a new approach to controllable molecular self-assembly, particularly for the systems where thermally-activated self-assembly is not feasible.

5.2 Methods

Sample and Tip Preparation

Sample preparation and STM measurements were performed in an ultrahigh vacuum system (base pressure is better than 1×10^{-10} mbar). Experiments were conducted with a home-built variable temperature scanning tunneling microscopy, whose temperature can vary from 25 K to 300 K. Phenylacetylene molecules were purified by the standard freeze-pump-thaw process. The Au(111) surface was cleaned by standard argon sputtering-annealing cycles before deposition of phenylacetylene molecules. The Au(111) substrate was kept at around 120 K during the molecular deposition. A commercial Pt-Ir tip was prepared by gentle field emission at a clean Au(111) sample. The bias voltage was applied on the sample during the STM observations. The STM images were analyzed using WsXM [91].

DFT calculations

Three sets of structures comprising a single molecule on Au were investigated with density functional theory (DFT). Each set contained several configurations. For phenylacetylene on Au we investigated 12 configurations, which are characterized by the position of the center of the phenyl with respect to the Au atoms of the first, second or third layer, and by the rotation angle of the alkyne tail. They are very similar to the configurations investigated by Bilic *et al.* [123] for benzene on M(111), M=Cu, Ag and Au, except that we have included 4 more configurations to account for different rotation angles of the alkyne tail. For both the styrene and the phenylvinylidene derivative on Au we investigated 4 configurations. They are labeled as FCC, HCP, TOP, and Bridge, and they are the same configurations as studied by Ford *et at.* [117]. Thus, in total 20 configurations were modeled. Each was relaxed using the projector augmented-wave pseudopotentials (PAW) method [49] with an energy cutoff of 400 eV, $3 \times 3 \times 1$ K-points grid, dipole corrections, and with the exchange correlation potential approximated by the Perdew, Burke and Ernzerhof approximation (PBE) [35]. The molecule and the first layer of Au were allowed to relax until the atomic forces were smaller than 0.02 eV/Å.

All the calculations were carried out with the software VASP [124]. For every configuration, the hexagonal unit cell had an in-plane lattice parameter a of 33.7 Å, and c/a ratio of 0.93. The vacuum space, which is about 27 Å, is large enough to ensure that periodic images do not interact with each other. The Au substrate was represented with 4 layers.

The ordered structure in Figure 5.4c was represented with a hexagonal supercell with an in-plane lattice parameter a 11.88 Å and axial ratio c/a 2.69. The vacuum space was kept as 13.5 Å from the top of the molecule to the bottom of the nearby image Au slab. The relaxation of this structure was carried with VASP using the PAW pseudopotentials and PBE with an

energy cutoff of 400 eV and a K-point mesh of $4 \times 4 \times 1$. The molecules and the first layer of Au were allowed to relax until the atomic forces were smaller than 0.02 eV/Å.

s

5.3 Results and Discussion

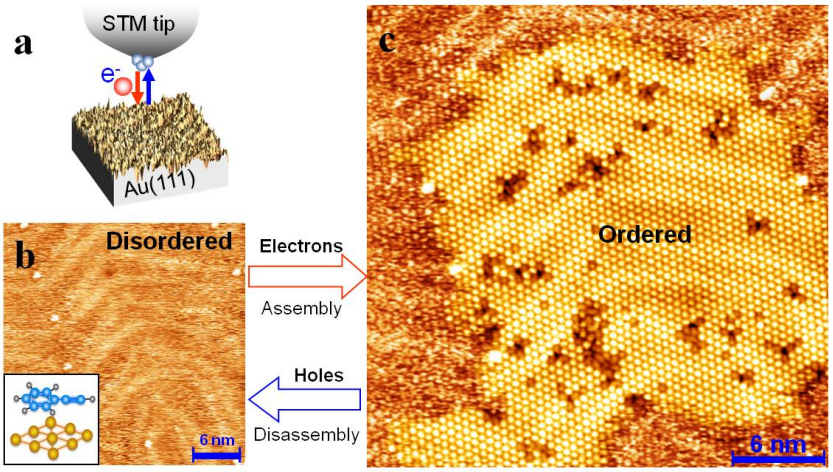

Figure 5.1: Transition between the disordered phase and the ordered phase by the tip induced reaction on the Au(111) surface. (a) Schematic drawing shows the experimental setup of the tip-induced reactions. (b) Topographic STM image of the disordered phase. Inserted figure is a schematic drawing of a flat-lying physisorbed phenylacetylene molecule. (c) Topographic STM image of ordered structure at the same location as (b) after the reaction.

Imaging the Au(111) surface by scanning tunneling microscopy (STM) after deposition of phenylacetylene at 85 K yields a fuzzy image with a clearly persistent topography of the $22 \times \sqrt{3}$ herringbone reconstruction (Figure 5.1b). The fuzziness indicates a mobile molecular overlayer [95, 125], in our case corresponding to physisorbed flat-lying phenylacetylene molecules on gold [76] (also see Appendix B, Figure B.1). The fuzzy STM image is dramatically transformed if the surface area is scanned by an STM tip with positive sample bias. As seen in Figure 5.1c, a clear ordered structure emerges (see Appendix B, Figure B.2), with an approximately hexagonal packing of molecular features. Once established, the ordered structure remains stable for a long period of time (over 24 hours), independent of tunneling conditions or even the presence of STM tip. The stability of the image indicates a different and stronger bonding between phenylacetylene molecules and the gold surface. At the same time, the underlying herringbone reconstruction is not lifted, indicating that the Au surface is not significantly perturbed in

the process, in stark contrast to the self-assembly of alkanethiols [126, 127]. The area of the surface that undergoes this disorder-order transition can be hundreds of square nanometers, accommodating thousands of ordered molecules (see Appendix B, Figure B.2). The process of building the ordered structure is dependent on the net injected charge, which can in turn be controlled by the scan rate of the STM tip. At the chosen sample bias of +1 V, the conversion is negligible at a scan rate exceeding 300 nm/s. By investigating the net assembly yield as a function of scan-rate, we derived a linear plot with a slope of 6.1×10^{-9} molecule/electron (Figure 5.2a). This is a rough estimate for a lower bound of the reaction yield under our specific imaging conditions, since we cannot resolve the molecules within the fuzzy image.

While injection of hot electrons causes the molecules to react and self-assemble, hot holes (supplied by negative sample bias) cause a highly controllable disassembly (Figure 5.2b). In this case, the STM tip does not have to raster the image. Instead, hot holes are injected into the surface from a single position under the tip, and disassembly occurs in a large area surrounding the tip-surface junction, as seen in a series of images in Figure 5.2b. Disassembly is always initiated at the periphery of the ordered structure and proceeds inward to the center. Once the disassembling front reaches the tunnel junction, the tunneling current drops to zero (the plot of recording tunneling current *vs.* time in Figure 5.2c), indicating the conversion of the molecules under the tip. The order-disorder transition is completely reversible in the same area of the surface, allowing one to create, erase and recreate the ordered structures simply by varying the tunneling conditions and scan parameters, as shown in a series of consecutive STM images in Figure 5.2d. This level of control over the self-assembly/disassembly processes provided by electron/hole induced reactions is largely unprecedented. The molecule density of ordered structure is apparently higher than that of the disordered phase. Extra molecules can be supplied either by molecular diffusion on gold surface or deposition from the tip. A complete reversibility of the process strongly argues that diffusion on gold is the dominant process in this case.

The reversibility of the self-assembly process (Figure 5.2d) strongly argues that the phenylacetylene molecule maintains its stoichiometry during the disorder-order transition. According to previous reports [117], phenylacetylene molecules have flat-lying and upright configurations on metal surfaces. Particularly, the intermolecular interactions between flat-lying molecule could only be attractive for six nearest-neighbor molecules with an intermolecular spacing of $\sim$8 Å on Au(111) surface [76]. In contrast, the self-assembled layer in Figure 5.3a is composed of hundreds of molecules, arranged with well-defined translational symmetry, and a nearest neighbor distance of about 6.15 Å. Since neither the continuous packing, nor the packing density of the self-assembled layer is compatible with the flat-lying orientation, we assign the building blocks to phenylacetylene derivatives with upright orientation of the phenyl ring.

The upright orientation of the molecule is directly supported by our low temperature exper-

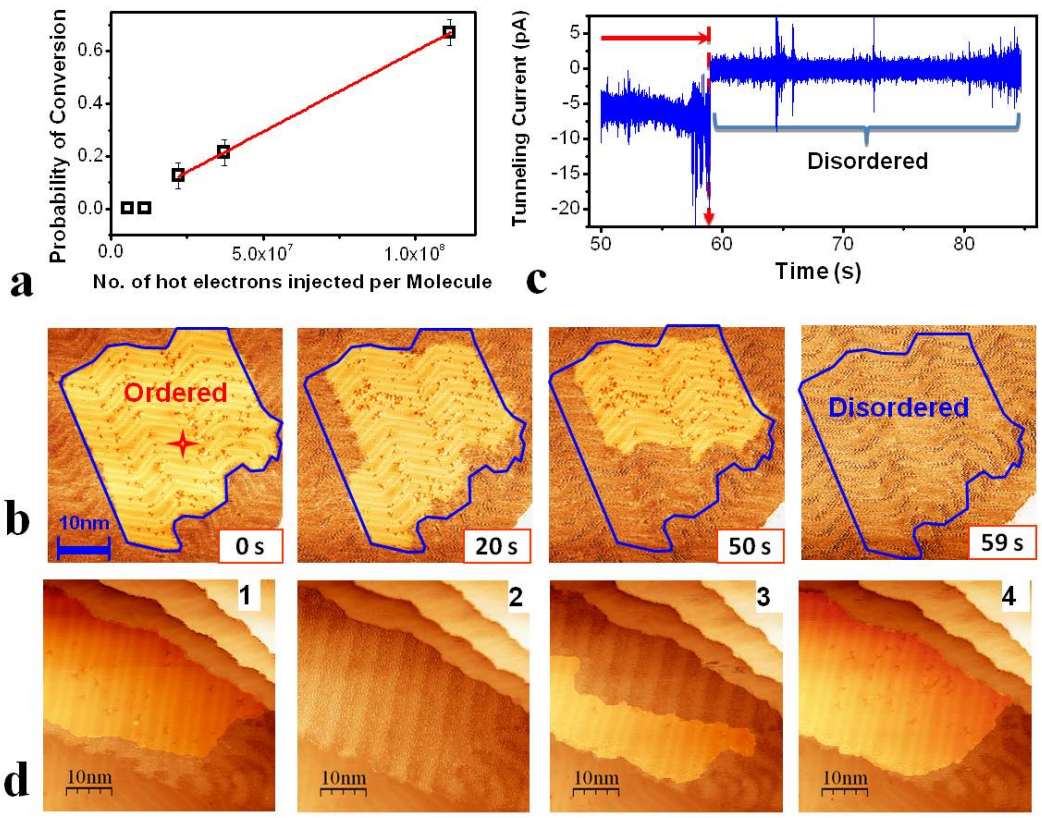

Figure 5.2: Electron-induced controllable and reversible transition between the order and disorder phase. (a) The probability of conversion from the disordered to ordered configuration *vs.* the average number of electrons injected per molecule. The tunneling junction was set with a sample bias of +1.6 V and tunneling current of 50 pA. (b) A series of images (V_{bias} = +1 V, I_{set} = 30 pA) showing snapshots of disassembly process after 0 s, 20 s, 50 s and 59 s of hole-injection into the surface, using voltage pulses at −0.5 V sample bias. A star in the image of 0 s indicates the location on the surface where the negative pulses were applied. (c) Time-dependence of the tunneling current signal during the disassembly process, showing an abrupt drop of current when the ordered domain completely disappears. (d) A series of subsequent images showing the reproducibility and controllability of the phase transition. The ordered structures emerge by slow scanning with a positive bias voltage and the self-assembled layer is destroyed by a negative bias pulse. The bias voltage during scanning (30 nm/s) is set at +1 V and the tunneling current is 20 pA. The negative bias here is −0.6 V.

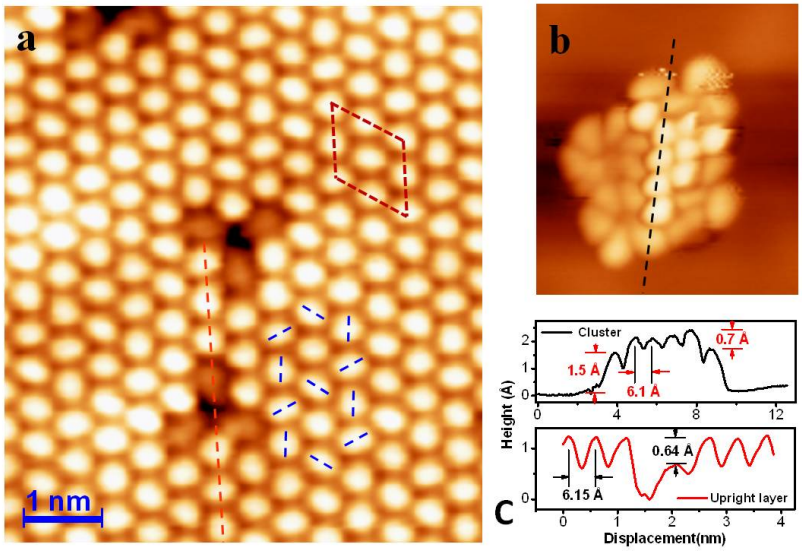

Figure 5.3: Evidence of the flat-lying and upright orientations of the molecule in the disordered and ordered phase. (a) Highly resolved STM image ($V_{bias} = +1.6$ V, $I_{set} = 50$ pA) of the ordered structure. The dashed lines indicate the pinwheel-like structure of ordered molecules, originated from the T-junction of the upright phenyl rings. Red rhombus shows the unit cell of the ordered structure. (b) A highly resolved STM image acquired at 28 K show the coexistence of flat-lying and upright molecule species. The upright molecules form similar hexagonal packing in both size and orientation with the ordered phase shown in (a). The flat-lying molecules have a well-known height of 1.5 Å and an elongated shape, similar to the defect in (a). (c) Line profiles across the defect of (a) and along the island in (b).

iments carried out at 28 K, at which the molecules with both orientations are stabilized. After imaging phenylacetylene at a bias of +1 V (Figure 5.3b), we observed the flat-lying species (dark) and reacted (bright) molecules. The STM apparent height between the flat-lying and reacted ones is about 0.7 Å (Figure 5.3c), in good agreement with the height difference (0.8 Å) between flat-lying and upright molecules on Si(100) surface [128]. The reacted molecules are identical to the building blocks of the self-assembled phase at 85 K, with regard to the shape of the molecular features and their similar hexagonal packing in both size and orientation. Meanwhile, the flat-lying molecules, which is known to show an elongated shape and has a height of 1.5 Å [76], bear strong resemblance to the defects inside the self-assembled structure at 85 K, with also the 0.7 Å height difference (Figure 5.3a, c). Although a detailed analysis of the defects is outside the scope of the present discussion, the observed motion, emergence, and disappearance of the defects (see Appendix B, Figure B.3) clearly illustrates the transition between flat-lying and upright molecules at a single molecule level. Moreover, the low-temperature experiments confirmed the feasibility of attaching individual alkyne molecules to the gold surface.

Before considering dissociated alkyne groups as the anchor groups that attach pheylacetylene to gold, we have ascertained that undissociated upright phenylacetylene molecules cannot feasibly bond to the surface. The only binding interaction for the upright orientation in this case is the dipole-dipole interaction between the phenylacetylene (dipole moment of 0.656 D in the gas-phase [129]) and its image dipole. Our DFT calculations revealed that upright oriented, physisorbed phenylacetylene will evaporate from gold surface if only the dipole-dipole interaction is considered (see Appendix B).

Two candidate structures of the reacted alkyne group that tethers phenylacetylene derivatives to the gold surface are compatible with our observations, both similar to the structures proposed in Ref. (11). The first one involves partial dissociation of the triple bond and bonding with the C–C double bond approximately parallel to the surface (hereafter called styrene-derivative, Figure 5.4a). The second one involves tautomerization of the ethyne group, with the proton moving to the C2 position to form a bonded phenylvinylidene (Figure 5.4b). We have used density functional theory (DFT) to investigate 20 different configurations, including both of the above groups on different surface sites and the unreacted phenylacetylene (see Appendix B, Figure B.5 and Table B.1). Phenylvinylidene on Au(111) yields the overall largest binding energy (−421 meV), followed by the styrene derivative (−235 meV) and then phenylacetylene (−69 meV). In the most stable configuration of phenylvinylidene (Figure 5.4b), π-conjugation between the double-bond and the phenyl ring is maintained and the molecule is oriented normal to the surface. In contrast, the styrene derivate on Au(111) is tilted and its phenyl ring is significantly twisted (Figure 5.4a), both as a result of strong Pauli repulsion between the ortho-proton of the phenyl ring and the gold atoms of the surface.

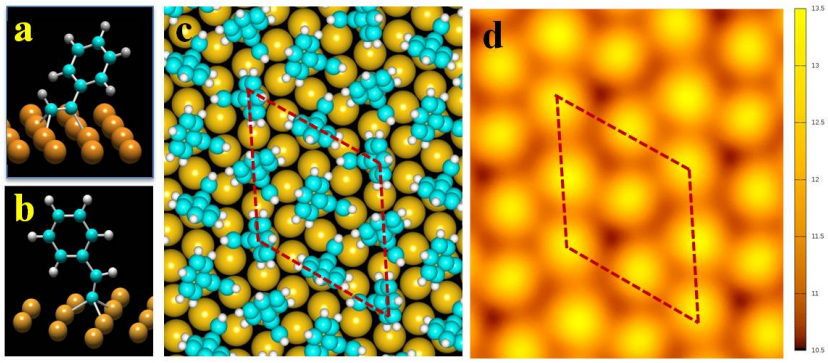

Figure 5.4: Structural model of the self-assembly monolayer as well as the simulated scanned image. (a) The relaxed model of a single styrene-derivative on Au(111). (b) The relaxed model of a single phenylvinylidene on Au(111). (c) Top view of DFT-relaxed model for the self-assembled molecular monolayer. (d) Simulated constant current image of the self-assembled monolayer.

The reversibility of the reaction (Figure 5.2d) rules out deprotonation [117] of phenylacetylene in the process. Indeed, styrene-derivative has been discussed and well accepted by previous work [119,120,128], as an upright structure for phenylacetylene adsorbed on Cu(1 0 0), Rh(100) and Cu(111) surfaces. Particular, on the Au(111) surface the formation of phenylvinylidene by tautomerization is not likely due to the observed small height difference (0.7 Å). We thus composed a structural model for the ordered phase by placing upright styrene derivatives in a compact arrangement within the layer, with the phenyl rings rotated by at least 60° relative to each other. The structure relaxed by DFT is shown in Figure 5.4c. The distance between the nearest neighbors ranges between 5.09 Å to 6.74 Å, very close to the experimental value of 6.15 Å. The simulated constant current image (Figure 5.4d) matches the STM topographic image (Figure 5.3a) very well, both indicating the "pinwheel-like" structure, which implies a "T-like" junction between molecules. The "T-like", junctions demonstrated in Figure 5.4c, originate from CH/π hydrogen bonding between upright phenyl rings, which never happens between flat-lying ones. Such junctions are well known for aromatic molecules, including phenylacetylene derivatives [117]. The energy gain of 0.5–2 kcal/mol per junction [85] naturally explains the origin of the attractive interactions within the self-assembled layer.

The conversion of phenylacetylene to styrene derivative on Au is borderline favorable energetically with the reaction enthalpy of only -156 meV (see Appendix B, Table B.1). However, breaking of the alkyne bond in phenylacetylene to form styrene derivative is inevitably associated with a large activation barrier [117], which explains why phenylacetylene does not form upright self-assemblies on gold by thermal activation at any temperature below the desorption

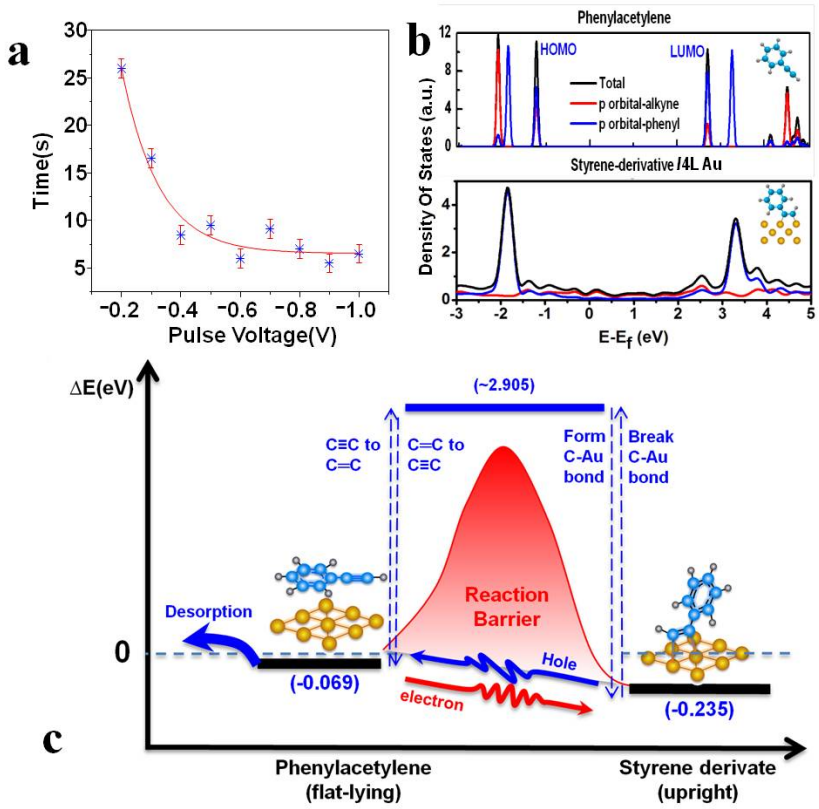

Figure 5.5: The Low energy threshold of the hot-hole induced reaction as well as its origin. (a) Pulse voltage dependence of the disassembly time at fixed gap distance ($V_{bias} = +1$ V, $I_{set} = 30$ pA). The error bars account for the scatter in the sizes of the ordered and disordered islands. This dependence can be phenomenologically fitted by exponential decay (red curve) with a threshold of about -0.2 V. (b) Calculated PDOS for two molecular configurations : gas-phase phenylacetylene and styrene-derivative on four layers of Au. The corresponding structures are shown in the right corner of each plot. All PDOS plots are aligned according to deep filled states. (c) Schematic illustration of the relevant energies for non-thermal reaction pathways of assembly/disassembly processes. ΔE is the binding energy.

threshold. A schematic in Figure 5.5c shows the relevant energies of the ground-state configurations relative to the flat-lying phenylacetylene molecules. Tip-induced hot electrons/holes injection overcome high reaction energy barriers, which prevent the reaction occurring by thermal pathways.

The hot electron energy threshold for the assembly process was estimated to be +0.3–0.4 eV by quantifying the size of the self-assembled structures as a function of scan rate (Figure 5.2a), comparable to the C≡C stretch modes of the gas-phase phenylacetylene molecule that have energy of 264 meV [130] from our DFT calculations. Therefore, the assembly reaction is most likely initiated by the vibrationally-excited phenylacetylene in its ground electronic state, which is a common mechanism for STM-induced chemistry [131, 132]. This mechanism is consistent with the comparatively low reaction yield for the assembly reaction, and the fact that the lowest unoccupied molecular orbital (LUMO) of adsorbed phenylacetylene is centered at least 2.5 eV above the Fermi level [76], precluding electron attachment at the tunneling bias of 0.4 V. At present we cannot rule out tip-assistance in this reaction, due to attraction and polarization of the flat-lying molecule by the field and/or chemical forces [115].

The disassembly at a distance proceeds through a more intriguing mechanism of delocalized excitation, which was recently reported for a number of molecules on metal surfaces [133]. In almost all the cases, the reactions were induced by reactive electron attachment of hot electrons that propagate *via* the surface resonances of the metal surfaces [133–135]. The estimated net yield of the reaction is 6.3×10^{-7} molecule per electron (see Appendix B, Figure B.4), at least two orders of magnitude higher than that for the assembly reaction and consistent with the relevant range for delocalized reactions. One can thus disassemble thousands of molecules in mesoscopic surface areas in a matter of minutes (see Appendix B, Figure B.4). The energy threshold for the hot-hole induced reaction in our case is around −0.2 eV, as seen in Figure 5.5a, which necessitates that the molecular highest occupied molecular orbital (HOMO) is in this energy range. Theoretical calculations of styrene-derivative support this view (Figure 5.5b and Appendix B, Figure B.6). Indeed, not only is the HOMO of styrene derivative strongly broadened, but its HOMO–LUMO gap is also very narrow. The HOMO does closely approaches the Fermi level of the Au surface. Injecting holes into this orbital will destabilize the Au–C bonds, thus initiating the untethering of the molecules and by extension the disassembly reaction.

5.4 Conclusion

We have demonstrated a non-thermal control over attachment and subsequent self-assembly of phenylacetylene into a well-ordered three-dimensional monolayer on the gold surface. Electron-induced self-assembly does not change the stoichiometry of the parent phenylacetylene molecule

and does not significantly perturb the underlying metal surface, while creating robust and strong chemical bonds at the metal-molecule interface. Moreover, the reaction is completely controllable and reversible, allowing us to manipulate the self-assembled layer from single molecule to mesoscopic scale. From a broader perspective, the electrons assisted direct control over the anchor bond chemistry has allowed us to self-assemble molecules that do not or even cannot self-assemble by thermal activation. We envision that in the future, excitation with light, macroscopic electron beams or a combination of the two can be invoked to gain local and global control over the self-assembly without thermal excitation, allowing for new chemical design rules aimed at self-assembly of small and large molecules on demand and in a desired pattern for electronic, photonic and energy applications.

Chapter 6

Further Perspectives and Future Work

In this thesis, we have investigated the STM patterns of graphene nanoflakes and phenylacetylene self-assembly processes on Au(111) surface. Our DFT simulations provide detailed atomic configurations and electronic structures of those experimental observations, and suggest the underlying physical mechanisms governing those processes.

There are several factors to consider in future work. In STM observations of graphene nanoflakes, substrates or STM tips could exert substantial influences on electron interference patterns. Specifically, a graphene flake is very flexible and capable of being bent by an STM tip. It is reported that an STM tip could push the graphene films under the tip toward the substrate by 0.5 Å [2], while the equilibrium distance between graphene and substrate is typically only 3.0 Å for a physisorbed sample. The mechanically bent graphene might have a different interference pattern, comparing to our current results.

Many interesting physics issues are found in phenylacetylene self-assembly processes on Au(111) surface. Several follow up studies have been done since our first publication on CH/π bonded 2D supramolecules [136–138]. It is reasonable to generalize those observations to different metal surfaces or different molecules. The substrate substantially influences the geometry of the weakly bonded phenylacetylene supramolecules, since the supramolecules have the same symmetry as the Au(111) surface. Intuitively, tetramer structures with $C4$ symmetry are likely to be observed on an inert surface with $C4$ symmetry. Furthermore, similar molecule-state splitting is possible in the new cluster geometries. Other molecules might have a similar self-assembly process [137], and other intermolecular bonds are possible besides CH/π bond [138].

Finally, it would be of particular interest and importance if we could find other molecules with similar electronically-controllable self-assembly processes. The phenylacetylene molecules are the first in the literature to be manipulated by STM tips to form reversible self-assembled

structures. The high activation barrier to self-assembly is overcome by the STM carrier injection. Therefore, the self-assembly can take place at the desired place and time. This is very attractive to many engineering processes, and worthy of serious screening of candidate molecules.

REFERENCES

[1] K. A. Ritter and J. W. Lyding, "The influence of edge structure on the electronic properties of graphene quantum dots and nanoribbons," *Nature Materials*, vol. 8, pp. 235–242, Feb. 2009.

[2] K. T. He, J. C. Koepke, S. Barraza-Lopez, and J. W. Lyding, "Separation-Dependent Electronic Transparency of Monolayer Graphene Membranes on IIIV Semiconductor Substrates," *Nano Letters*, vol. 10, no. 9, pp. 3446–3452, 2010.

[3] R. Parr and Y. Weitao, *Density-Functional Theory of Atoms and Molecules*. International Series of Monographs on Chemistry, Oxford University Press, USA, 1994.

[4] R. Martin, *Electronic Structure: Basic Theory and Practical Methods*. Cambridge University Press, 2004.

[5] E. Gross and R. Dreizler, *Density Functional Theory*. NATO ASI Series: Physics, Springer, 1995.

[6] R. Nalewajski, *Perspectives in Electronic Structure Theory*. Springer, 2012.

[7] C. Fiolhais, F. Nogueira, and M. Marques, *A Primer in Density Functional Theory*. Lecture Notes in Physics, Springer, 2003.

[8] P. Politzer and J. Seminario, *Modern Density Functional Theory: A Tool For Chemistry*. Theoretical and Computational Chemistry, Elsevier Science, 1995.

[9] J. M. Seminario, *Recent Developments And Applications Of Modern Density Functional Theory*. Theoretical and Computational Chemistry, Elsevier, 1996.

[10] M. Born and R. Oppenheimer, "Zur Quantentheorie der Molekeln," *Annalen der Physik*, vol. 389, no. 20, pp. 457–484, 1927.

[11] D. R. Hartree, "The Wave Mechanics of an Atom with a Non-Coulomb Central Field. Part II. Some Results and Discussion," *Mathematical Proceedings of the Cambridge Philosophical Society*, vol. 24, no. 01, pp. 111–132, 1928.

[12] J. C. Slater, "A Simplification of the Hartree-Fock Method," *Physical Review*, vol. 81, pp. 385–390, Feb. 1951.

[13] L. H. Thomas, "The calculation of atomic fields," *Mathematical Proceedings of the Cambridge Philosophical Society*, vol. 23, no. 05, pp. 542–548, 1927.

[14] E. Fermi, "Un metodo statistico per la determinazione di alcune priorieta dell'atome," *Rend. Accad. Naz. Lincei*, vol. 6, no. 05, p. 602607, 1927.

[15] P. a. M. Dirac, "Note on Exchange Phenomena in the Thomas Atom," *Mathematical Proceedings of the Cambridge Philosophical Society*, vol. 26, no. 03, pp. 376–385, 1930.

[16] P. Hohenberg and W. Kohn, "Inhomogeneous Electron Gas," *Physical Review*, vol. 136, pp. B864–B871, Nov. 1964.

[17] W. Kohn and L. J. Sham, "Self-Consistent Equations Including Exchange and Correlation Effects," *Physical Review*, vol. 140, pp. A1133–A1138, Nov. 1965.

[18] J. F. Janak, "Proof that $\partial \mathrm{E}/\partial n_i = \varepsilon$ in density-functional theory," *Phys. Rev. B*, vol. 18, pp. 7165–7168, Dec 1978.

[19] C.-O. Almbladh and U. von Barth, "Exact results for the charge and spin densities, exchange-correlation potentials, and density-functional eigenvalues," *Physical Review B*, vol. 31, pp. 3231–3244, Mar. 1985.

[20] J. Tao, J. P. Perdew, V. N. Staroverov, and G. E. Scuseria, "Climbing the Density Functional Ladder: Nonempirical Meta˘Generalized Gradient Approximation Designed for Molecules and Solids," *Phys. Rev. Lett.*, vol. 91, p. 146401, Sep 2003.

[21] D. M. Bylander and L. Kleinman, "Optimized effective potentials for semiconductors," *Phys. Rev. B*, vol. 52, pp. 14566–14570, Nov 1995.

[22] J. P. Perdew and M. Levy, "Physical Content of the Exact Kohn-Sham Orbital Energies: Band Gaps and Derivative Discontinuities," *Physical Review Letters*, vol. 51, pp. 1884–1887, Nov. 1983.

[23] L. J. Sham and M. Schlüter, "Density-Functional Theory of the Energy Gap," *Physical Review Letters*, vol. 51, pp. 1888–1891, Nov. 1983.

[24] D. M. Ceperley and B. J. Alder, "Ground State of the Electron Gas by a Stochastic Method," *Phys. Rev. Lett.*, vol. 45, pp. 566–569, Aug 1980.

[25] J. P. Perdew and A. Zunger, "Self-interaction correction to density-functional approximations for many-electron systems," *Physical Review B*, vol. 23, p. 5048, May 1981.

[26] J. P. Perdew and Y. Wang, "Pair-distribution function and its coupling-constant average for the spin-polarized electron gas," *Physical Review B*, vol. 46, pp. 12947–12954, Nov. 1992.

[27] R. O. Jones and O. Gunnarsson, "The density functional formalism, its applications and prospects," *Reviews of Modern Physics*, vol. 61, pp. 689–746, July 1989.

[28] J. Harris and R. O. Jones, "The surface energy of a bounded electron gas," *Journal of Physics F: Metal Physics*, vol. 4, no. 8, p. 1170, 1974.

[29] F. Herman, J. P. Van Dyke, and I. B. Ortenburger, "Improved Statistical Exchange Approximation for Inhomogeneous Many-Electron Systems," *Physical Review Letters*, vol. 22, pp. 807–811, Apr. 1969.

[30] P. S. Svendsen and U. von Barth, "Gradient expansion of the exchange energy from second-order density response theory," *Physical Review B*, vol. 54, pp. 17402–17413, Dec. 1996.

[31] D. C. Langreth and J. P. Perdew, "Theory of nonuniform electronic systems. I. Analysis of the gradient approximation and a generalization that works," *Physical Review B*, vol. 21, pp. 5469–5493, June 1980.

[32] J. P. Perdew and W. Yue, "Accurate and simple density functional for the electronic exchange energy: Generalized gradient approximation," *Physical Review B*, vol. 33, pp. 8800–8802, June 1986.

[33] J. Perdew, "Unified Theory of Exchange and Correlation Beyond the Local Density Approximation," in *Electronic Structure of Solids'91* (P. Ziesche and H. Eschrig, eds.), pp. 11–20, Akademie Verlag, Berlin, 1991.

[34] K. Burke, J. P. Perdew, and Y. Wang, *Electronic Density Functional Theory: Recent Progress and New Directions*. NY: Plenum, 1997.

[35] J. P. Perdew, K. Burke, and M. Ernzerhof, "Generalized gradient approximation made simple," *Physical Review Letters*, vol. 77, p. 3865, Oct. 1996.

[36] J. P. Perdew, K. Burke, and M. Ernzerhof, "Generalized Gradient Approximation Made Simple [Phys. Rev. Lett. 77, 3865 (1996)]," *Physical Review Letters*, vol. 78, p. 1396, Feb. 1997.

[37] A. D. Becke, "Density-functional exchange-energy approximation with correct asymptotic behavior," *Physical Review A*, vol. 38, pp. 3098–3100, Sept. 1988.

[38] C. Lee, W. Yang, and R. G. Parr, "Development of the Colle-Salvetti correlation-energy formula into a functional of the electron density," *Physical Review B*, vol. 37, pp. 785–789, Jan. 1988.

[39] V. I. Anisimov, F. Aryasetiawan, and A. I. Lichtenstein, "First-principles calculations of the electronic structure and spectra of strongly correlated systems: the LDA + U method," *Journal of Physics: Condensed Matter*, vol. 9, pp. 767–808, Jan. 1997.

[40] V. I. Anisimov, J. Zaanen, and O. K. Andersen, "Band theory and Mott insulators: Hubbard U instead of Stoner I," *Physical Review B*, vol. 44, pp. 943–954, July 1991.

[41] M. Dion, H. Rydberg, E. Schröder, D. C. Langreth, and B. I. Lundqvist, "Van der Waals Density Functional for General Geometries," *Physical Review Letters*, vol. 92, p. 246401, June 2004.

[42] K. Lee, É. D. Murray, L. Kong, B. I. Lundqvist, and D. C. Langreth, "Higher-accuracy van der Waals density functional," *Physical Review B*, vol. 82, no. 8, p. 081101, 2010.

[43] C. Herring, "A New Method for Calculating Wave Functions in Crystals," *Physical Review*, vol. 57, pp. 1169–1177, June 1940.

[44] C. Herring and A. G. Hill, "The Theoretical Constitution of Metallic Beryllium," *Physical Review*, vol. 58, pp. 132–162, July 1940.

[45] W. Pickett, *Pseudopotential Methods in Condensed Matter Applications*. North-Holland, 1989.

[46] D. R. Hamann, M. Schlüter, and C. Chiang, "Norm-Conserving Pseudopotentials," *Physical Review Letters*, vol. 43, pp. 1494–1497, Nov. 1979.

[47] D. Vanderbilt, "Soft self-consistent pseudopotentials in a generalized eigenvalue formalism," *Physical Review B*, vol. 41, p. 7892, Apr. 1990.

[48] P. E. Blöchl, "Generalized separable potentials for electronic-structure calculations," *Physical Review B*, vol. 41, pp. 5414–5416, Mar. 1990.

[49] P. E. Blöchl, "Projector augmented-wave method," *Physical Review B*, vol. 50, pp. 17953–17979, Dec. 1994.

[50] G. Kresse and D. Joubert, "From ultrasoft pseudopotentials to the projector augmented-wave method," *Physical Review B*, vol. 59, p. 1758, Jan. 1999.

[51] N. A. W. Holzwarth, G. E. Matthews, R. B. Dunning, A. R. Tackett, and Y. Zeng, "Comparison of the projector augmented-wave, pseudopotential, and linearized augmented-plane-wave formalisms for density-functional calculations of solids," *Physical Review B*, vol. 55, pp. 2005–2017, Jan. 1997.

[52] T. L. Beck, "Real-space mesh techniques in density-functional theory," *Reviews of Modern Physics*, vol. 72, pp. 1041–1080, Oct. 2000.

[53] J. R. Chelikowsky, N. Troullier, and Y. Saad, "Finite-difference-pseudopotential method: Electronic structure calculations without a basis," *Physical Review Letters*, vol. 72, pp. 1240–1243, Feb. 1994.

[54] E. L. Briggs, D. J. Sullivan, and J. Bernholc, "Large-scale electronic-structure calculations with multigrid acceleration," *Physical Review B*, vol. 52, pp. R5471–R5474, Aug. 1995.

[55] E. L. Briggs, D. J. Sullivan, and J. Bernholc, "Real-space multigrid-based approach to large-scale electronic structure calculations," *Physical Review B*, vol. 54, no. 20, pp. 14362–14375, 1996.

[56] R. D. King-Smith, M. C. Payne, and J. S. Lin, "Real-space implementation of nonlocal pseudopotentials for first-principles total-energy calculations," *Physical Review B*, vol. 44, no. 23, pp. 13063–13066, 1991.

[57] J. Tersoff and D. R. Hamann, "Theory of the scanning tunneling microscope," *Physical Review B*, vol. 31, p. 805, Jan. 1985.

[58] A. K. Geim and K. S. Novoselov, "The rise of graphene," *Nature Materials*, vol. 6, no. 3, pp. 183–191, 2007.

[59] A. H. Castro Neto, F. Guinea, N. M. R. Peres, K. S. Novoselov, and A. K. Geim, "The electronic properties of graphene," *Reviews of Modern Physics*, vol. 81, pp. 109–162, Jan. 2009.

[60] K. S. Novoselov, "Electric field effect in atomically thin carbon films," *Science*, vol. 306, pp. 666–669, Oct. 2004.

[61] J. Tersoff, "Anomalous corrugations in scanning tunneling microscopy: Imaging of individual states," *Physical Review Letters*, vol. 57, pp. 440–443, July 1986.

[62] G. M. Rutter, J. N. Crain, N. P. Guisinger, T. Li, P. N. First, and J. A. Stroscio, "Scattering and interference in epitaxial graphene," *Science*, vol. 317, pp. 219–222, July 2007.

[63] G. M. Shedd and P. E. Russell, "A simple wave function interference model for the electron-density superstructures observed during scanning tunneling microscopy of perturbed graphite surfaces," *Surface science*, vol. 266, no. 1-3, p. 259264, 1992.

[64] H. A. Mizes, "The signature of point defects in layered materials," *Journal of Vacuum Science & Technology A: Vacuum, Surfaces, and Films*, vol. 6, p. 300, Mar. 1988.

[65] Y. Ferro and A. Allouche, "Interpretation of STM images of graphite with an atomic vacancy via density-functional calculations of electronic structure," *Physical Review B*, vol. 75, p. 155438, Apr. 2007.

[66] K. Nakada, M. Fujita, G. Dresselhaus, and M. S. Dresselhaus, "Edge state in graphene ribbons: Nanometer size effect and edge shape dependence," *Physical Review B*, vol. 54, pp. 17954–17961, Dec. 1996.

[67] Y. Niimi, T. Matsui, H. Kambara, K. Tagami, M. Tsukada, and H. Fukuyama, "Scanning tunneling microscopy and spectroscopy studies of graphite edges," *Applied Surface Science*, vol. 241, pp. 43–48, Feb. 2005.

[68] Y. Niimi, T. Matsui, H. Kambara, K. Tagami, M. Tsukada, and H. Fukuyama, "Scanning tunneling microscopy and spectroscopy of the electronic local density of states of graphite surfaces near monoatomic step edges," *Physical Review B*, vol. 73, p. 085421, Feb. 2006.

[69] E. Cisternas, F. Stavale, M. Flores, C. Achete, and P. Vargas, "First-principles calculation and scanning tunneling microscopy study of highly oriented pyrolytic graphite (0001)," *Physical Review B*, vol. 79, May 2009.

[70] Y. Kobayashi, K.-i. Fukui, T. Enoki, and K. Kusakabe, "Edge state on hydrogen-terminated graphite edges investigated by scanning tunneling microscopy," *Physical Review B*, vol. 73, p. 125415, Mar. 2006.

[71] K.-i. Sakai, K. Takai, K.-i. Fukui, T. Nakanishi, and T. Enoki, "Honeycomb superperiodic pattern and its fine structure near the armchair edge of graphene observed by low-temperature scanning tunneling microscopy," *Physical Review B*, vol. 81, p. 235417, June 2010.

[72] E. Stolyarova, K. T. Rim, S. Ryu, J. Maultzsch, P. Kim, L. E. Brus, T. F. Heinz, M. S. Hybertsen, and G. W. Flynn, "High-resolution scanning tunneling microscopy imaging of mesoscopic graphene sheets on an insulating surface," *Proceedings of the National Academy of Sciences*, vol. 104, no. 22, p. 9209, 2007.

[73] D. Tomnek, S. G. Louie, H. J. Mamin, D. W. Abraham, R. E. Thomson, E. Ganz, and J. Clarke, "Theory and observation of highly asymmetric atomic structure in scanning-tunneling-microscopy images of graphite," *Physical Review B*, vol. 35, p. 7790, May 1987.

[74] Y.-W. Son, M. L. Cohen, and S. G. Louie, "Energy gaps in graphene nanoribbons," *Physical Review Letters*, vol. 97, p. 216803, Nov. 2006.

[75] M. Igami, K. Nakada, and Fujita, "Lattice distortion in nanographite ribbons," *Journal of the Physical Society of Japan*, vol. 66, no. 7, pp. 1864–1867.

[76] Q. Li, C. Han, S. R. Horton, M. Fuentes-Cabrera, B. G. Sumpter, W. Lu, J. Bernholc, P. Maksymovych, and M. Pan, "Supramolecular Self-Assembly of π-Conjugated Hydrocarbons via 2D Cooperative CH/π Interaction," *ACS Nano*, vol. 6, pp. 566–572, Jan. 2012.

[77] L. Bartels, "Tailoring molecular layers at metal surfaces," *Nat Chem*, vol. 2, pp. 87–95, Feb. 2010.

[78] W. A. de Heer, "The physics of simple metal clusters: experimental aspects and simple models," *Reviews of Modern Physics*, vol. 65, pp. 611–676, July 1993.

[79] T. Yokoyama, S. Yokoyama, T. Kamikado, Y. Okuno, and S. Mashiko, "Selective assembly on a surface of supramolecular aggregates with controlled size and shape," *Nature*, vol. 413, pp. 619–621, Oct. 2001.

[80] M. Böhringer, K. Morgenstern, W.-D. Schneider, R. Berndt, F. Mauri, A. De Vita, and R. Car, "Two-Dimensional Self-Assembly of Supramolecular Clusters and Chains," *Physical Review Letters*, vol. 83, pp. 324–327, July 1999.

[81] D. Heim, K. Seufert, W. Auwärter, C. Aurisicchio, C. Fabbro, D. Bonifazi, and J. V. Barth, "Surface-Assisted Assembly of Discrete Porphyrin-Based Cyclic Supramolecules," *Nano Letters*, vol. 10, pp. 122–128, Jan. 2010.

[82] G. C. Pimentel and A. L. McClellan, "Hydrogen Bonding," *Annual Review of Physical Chemistry*, vol. 22, no. 1, pp. 347–385, 1971.

[83] J. Weckesser, A. De Vita, J. V. Barth, C. Cai, and K. Kern, "Mesoscopic Correlation of Supramolecular Chirality in One-Dimensional Hydrogen-Bonded Assemblies," *Physical Review Letters*, vol. 87, p. 096101, Aug. 2001.

[84] G. R. Desiraju and T. Steiner, *The Weak Hydrogen Bond: In Structural Chemistry and Biology*. Oxford University Press, Aug. 2001.

[85] M. Nishio, "CH/π hydrogen bonds in crystals," *CrystEngComm*, vol. 6, no. 27, p. 130, 2004.

[86] S. Kumar, K. Subramanian, R. Srinivasan, K. Rajagopalan, A. Schreurs, J. Kroon, and T. Steiner, "N-(p-methoxyphenyl)-N-prop-2-ynyl-urea: a crystal structure with the rare Z=5, and statistical data on Z values," *Journal of Molecular Structure*, vol. 520, pp. 131–139, Mar. 2000.

[87] I. Fernandez-Torrente, K. J. Franke, N. Henningsen, G. Schulze, M. Alemani, C. Roth, R. Rurali, N. Lorente, and J. I. Pascual, "Spontaneous Formation of Triptycene Supramolecules on Surfaces," *The Journal of Physical Chemistry B*, vol. 110, pp. 20089–20092, Oct. 2006.

[88] M. Pivetta, M.-C. Blüm, F. Patthey, and W.-D. Schneider, "Two-Dimensional Tiling by Rubrene Molecules Self-Assembled in Supramolecular Pentagons, Hexagons, and Heptagons on a Au(111) Surface," *Angewandte Chemie*, vol. 120, no. 6, pp. 1092–1095, 2008.

[89] E. C. H. Sykes, B. A. Mantooth, P. Han, Z. J. Donhauser, and P. S. Weiss, "Substrate-Mediated Intermolecular Interactions: A Quantitative Single Molecule Analysis," *Journal of the American Chemical Society*, vol. 127, pp. 7255–7260, May 2005.

[90] D. B. Dougherty, W. Jin, W. G. Cullen, J. E. Reutt-Robey, and S. W. Robey, "Variable Temperature Scanning Tunneling Microscopy of Pentacene Monolayer and Bilayer Phases on Ag(111)," *The Journal of Physical Chemistry C*, vol. 112, pp. 20334–20339, Dec. 2008.

[91] I. Horcas, R. Fernández, J. M. Gómez-Rodríguez, J. Colchero, J. Gómez-Herrero, and A. M. Baro, "WSXM: A software for scanning probe microscopy and a tool for nanotechnology," *Review of Scientific Instruments*, vol. 78, pp. 013705–013705–8, Jan. 2007.

[92] P. Giannozzi, S. Baroni, N. Bonini, M. Calandra, R. Car, C. Cavazzoni, D. Ceresoli, G. L. Chiarotti, M. Cococcioni, I. Dabo, A. Dal Corso, S. de Gironcoli, S. Fabris, G. Fratesi, R. Gebauer, U. Gerstmann, C. Gougoussis, A. Kokalj, M. Lazzeri, L. Martin-Samos, N. Marzari, F. Mauri, R. Mazzarello, S. Paolini, A. Pasquarello, L. Paulatto, C. Sbraccia, S. Scandolo, G. Sclauzero, A. P. Seitsonen, A. Smogunov, P. Umari, and R. M. Wentzcovitch, "QUANTUM ESPRESSO: a modular and open-source software project for quantum simulations of materials," *Journal of Physics: Condensed Matter*, vol. 21, p. 395502, Sept. 2009.

[93] L. Bengtsson, "Dipole correction for surface supercell calculations," *Physical Review B*, vol. 59, p. 12301, May 1999.

[94] R. A. Kendall, E. Aprà, D. E. Bernholdt, E. J. Bylaska, M. Dupuis, G. I. Fann, R. J. Harrison, J. Ju, J. A. Nichols, J. Nieplocha, T. Straatsma, T. L. Windus, and A. T. Wong, "High performance computational chemistry: An overview of NWChem a distributed parallel application," *Computer Physics Communications*, vol. 128, pp. 260–283, June 2000.

[95] P. Han, B. A. Mantooth, E. C. H. Sykes, Z. J. Donhauser, and P. S. Weiss, "Benzene on Au(111) at 4 K: Monolayer Growth and Tip-Induced Molecular Cascades," *Journal of the American Chemical Society*, vol. 126, pp. 10787–10793, Sept. 2004.

[96] T. Steiner, "Cooperative $C \equiv C - H \ldots C \equiv C - H$ interactions: crystal structure of DL-prop-2-ynylglycine and database study of terminal alkynes," *J. Chem. Soc., Chem. Commun.*, p. 95, 1995.

[97] A. E. Reed, L. A. Curtiss, and F. Weinhold, "Intermolecular interactions from a natural bond orbital, donor-acceptor viewpoint," *Chemical Reviews*, vol. 88, pp. 899–926, Sept. 1988.

[98] Z. H. Cheng, L. Gao, Z. T. Deng, N. Jiang, Q. Liu, D. X. Shi, S. X. Du, H. M. Guo, and H.-J. Gao, "Adsorption Behavior of Iron Phthalocyanine on Au(111) Surface at Submonolayer Coverage," *The Journal of Physical Chemistry C*, vol. 111, pp. 9240–9244, July 2007.

[99] P. Ruffieux, K. Palotás, O. Gröning, D. Wasserfallen, K. Müllen, W. A. Hofer, P. Gröning, and R. Fasel, "Site- and Orientation-Selective Anchoring of a Prototypical Molecular Building Block," *Journal of the American Chemical Society*, vol. 129, pp. 5007–5011, Apr. 2007.

[100] W. Chen, V. Madhavan, T. Jamneala, and M. F. Crommie, "Scanning Tunneling Microscopy Observation of an Electronic Superlattice at the Surface of Clean Gold," *Physical Review Letters*, vol. 80, pp. 1469–1472, Feb. 1998.

[101] W. Haiss, "Surface stress of clean and adsorbate-covered solids," *Reports on Progress in Physics*, vol. 64, pp. 591–648, May 2001.

[102] S. Grimme, "Semiempirical GGA-type density functional constructed with a long-range dispersion correction," *Journal of Computational Chemistry*, vol. 27, pp. 1787–1799, Nov. 2006.

[103] D. B. Dougherty, P. Maksymovych, J. Lee, and J. T. Yates, "Local Spectroscopy of Image-Potential-Derived States: From Single Molecules to Monolayers of Benzene on Cu(111)," *Physical Review Letters*, vol. 97, p. 236806, Dec. 2006.

[104] M. Feng, J. Zhao, and H. Petek, "Atomlike, Hollow-Core–Bound Molecular Orbitals of C60," *Science*, vol. 320, pp. 359–362, Apr. 2008.

[105] Q. Li, C. Han, M. Fuentes-Cabrera, H. Terrones, B. G. Sumpter, W. Lu, J. Bernholc, J. Yi, Z. Gai, A. P. Baddorf, P. Maksymovych, and M. Pan, "Electronic control over attachment and self-assembly of alkyne groups on gold," *ACS Nano*, vol. 6, pp. 9267–9275, Oct. 2012.

[106] F.-R. F. Fan, J. Yang, L. Cai, Price, S. M. Dirk, D. V. Kosynkin, Y. Yao, A. M. Rawlett, J. M. Tour, and A. J. Bard, "Charge Transport through Self-Assembled Monolayers of Compounds of Interest in Molecular Electronics," *Journal of the American Chemical Society*, vol. 124, pp. 5550–5560, May 2002.

[107] B. Mantooth and P. Weiss, "Fabrication, assembly, and characterization of molecular electronic components," *Proceedings of the IEEE*, vol. 91, pp. 1785 – 1802, Nov. 2003.

[108] D. S. Ginger, H. Zhang, and C. A. Mirkin, "The Evolution of Dip-Pen Nanolithography," *Angewandte Chemie International Edition*, vol. 43, no. 1, pp. 30–45, 2004.

[109] P. Fenter, A. Eberhardt, and P. Eisenberger, "Self-Assembly of n-Alkyl Thiols as Disulfides on Au(111)," *Science*, vol. 266, pp. 1216–1218, Nov. 1994.

[110] J. C. Love, L. A. Estroff, J. K. Kriebel, R. G. Nuzzo, and G. M. Whitesides, "Self-Assembled Monolayers of Thiolates on Metals as a Form of Nanotechnology," *Chemical Reviews*, vol. 105, pp. 1103–1170, Apr. 2005.

[111] C. Vericat, M. E. Vela, G. Benitez, P. Carro, and R. C. Salvarezza, "Self-assembled monolayers of thiols and dithiols on gold: new challenges for a well-known system," *Chemical Society Reviews*, vol. 39, no. 5, p. 1805, 2010.

[112] G. E. Poirier, "Characterization of Organosulfur Molecular Monolayers on Au(111) using Scanning Tunneling Microscopy," *Chemical Reviews*, vol. 97, pp. 1117–1128, June 1997.

[113] P. Maksymovych, O. Voznyy, D. B. Dougherty, D. C. Sorescu, and J. T. Yates Jr., "Gold adatom as a key structural component in self-assembled monolayers of organosulfur molecules on Au(1 1 1)," *Progress in Surface Science*, vol. 85, pp. 206–240, May 2010.

[114] F. Schreiber, "Structure and growth of self-assembling monolayers," *Progress in Surface Science*, vol. 65, pp. 151–257, Nov. 2000.

[115] M. Alemani, M. V. Peters, S. Hecht, K.-H. Rieder, F. Moresco, and L. Grill, "Electric Field-Induced Isomerization of Azobenzene by STM," *Journal of the American Chemical Society*, vol. 128, pp. 14446–14447, Nov. 2006.

[116] M. J. Comstock, N. Levy, A. Kirakosian, J. Cho, F. Lauterwasser, J. H. Harvey, D. A. Strubbe, J. M. J. Fréchet, D. Trauner, S. G. Louie, and M. F. Crommie, "Reversible Photomechanical Switching of Individual Engineered Molecules at a Metallic Surface," *Physical Review Letters*, vol. 99, p. 038301, July 2007.

[117] M. J. Ford, R. C. Hoft, and A. McDonagh, "Theoretical Study of Ethynylbenzene Adsorption on Au(111) and Implications for a New Class of Self-Assembled Monolayer," *The Journal of Physical Chemistry B*, vol. 109, pp. 20387–20392, Nov. 2005.

[118] M. A. Walsh, S. R. Walter, K. H. Bevan, F. M. Geiger, and M. C. Hersam, "Phenylacetylene One-Dimensional Nanostructures on the Si(100)-2 × 1:H Surface," *Journal of the American Chemical Society*, vol. 132, pp. 3013–3019, Mar. 2010.

[119] Y. Sohn, W. Wei, and J. M. White, "Phenylacetylene on Cu(111): Adsorption Geometry, Interfacial Electronic Structures and Thermal Chemistry," *The Journal of Physical Chemistry C*, vol. 111, pp. 5101–5110, Apr. 2007.

[120] G. Iucci, V. Carravetta, P. Altamura, M. Russo, G. Paolucci, A. Goldoni, and G. Polzonetti, "XPS, NEXAFS and theoretical study of phenylacetylene adsorbed on Cu(1 0 0)," *Chemical Physics*, vol. 302, pp. 43–52, July 2004.

[121] A. M. McDonagh, H. M. Zareie, M. J. Ford, C. S. Barton, M. Ginic-Markovic, and J. G. Matisons, "Ethynylbenzene Monolayers on Gold: A Metal-Molecule Binding Motif Derived from a Hydrocarbon," *Journal of the American Chemical Society*, vol. 129, pp. 3533–3538, Mar. 2007.

[122] T. S. S. Rao and S. Awasthi, "Oxidative cleavage of carbon-carbon triple bond - a review," *Journal of the Indian Chemical Society*, vol. 80, pp. 1129–1141, Dec. 2003.

[123] A. Bilić, J. R. Reimers, N. S. Hush, R. C. Hoft, and M. J. Ford, "Adsorption of Benzene on Copper, Silver, and Gold Surfaces," *Journal of Chemical Theory and Computation*, vol. 2, pp. 1093–1105, July 2006.

[124] G. Kresse and J. Hafner, "Ab initio molecular dynamics for liquid metals," *Physical Review B*, vol. 47, pp. 558–561, Jan. 1993.

[125] N. Jiang, Y. Y. Zhang, Q. Liu, Z. H. Cheng, Z. T. Deng, S. X. Du, H.-J. Gao, M. J. Beck, and S. T. Pantelides, "Diffusivity Control in Molecule-on-Metal Systems Using Electric Fields," *Nano Letters*, vol. 10, pp. 1184–1188, Apr. 2010.

[126] G. Yang and G.-y. Liu, "New Insights for Self-Assembled Monolayers of Organothiols on Au(111) Revealed by Scanning Tunneling Microscopy," *The Journal of Physical Chemistry B*, vol. 107, pp. 8746–8759, Aug. 2003.

[127] G. E. Poirier and E. D. Pylant, "The Self-Assembly Mechanism of Alkanethiols on Au(111)," *Science*, vol. 272, pp. 1145–1148, May 1996.

[128] O. Pluchery, R. Coustel, N. Witkowski, and Y. Borensztein, "Adsorption of Phenylacetylene on Si(100)-2 × 1: Kinetics and Structure of the Adlayer," *The Journal of Physical Chemistry B*, vol. 110, pp. 22635–22643, Nov. 2006.

[129] A. P. Cox, I. C. Ewart, and W. M. Stigliani, "Microwave spectrum, structure and dipole moment of phenylacetylene," *Journal of the Chemical Society, Faraday Transactions 2*, vol. 71, p. 504, 1975.

[130] "Phenylethyne - the NIST WebBook." http://webbook.nist.gov.

[131] W. Ho, "Single-molecule chemistry," *The Journal of Chemical Physics*, vol. 117, pp. 11033–11061, Dec. 2002.

[132] L. J. Lauhon and W. Ho, "Single-Molecule Chemistry and Vibrational Spectroscopy: Pyridine and Benzene on Cu(001)," *The Journal of Physical Chemistry A*, vol. 104, pp. 2463–2467, Mar. 2000.

[133] J. M. MacLeod, J. Lipton-Duffin, C. Fu, and F. Rosei, "Inducing Nonlocal Reactions with a Local Probe," *ACS Nano*, vol. 3, pp. 3347–3351, Nov. 2009.

[134] P. Maksymovych, D. B. Dougherty, X.-Y. Zhu, and J. T. Yates, "Nonlocal Dissociative Chemistry of Adsorbed Molecules Induced by Localized Electron Injection into Metal Surfaces," *Physical Review Letters*, vol. 99, p. 016101, July 2007.

[135] R. Nouchi, K. Masunari, T. Ohta, Y. Kubozono, and Y. Iwasa, "Ring of C_{60} Polymers Formed by Electron or Hole Injection from a Scanning Tunneling Microscope Tip," *Physical Review Letters*, vol. 97, p. 196101, Nov. 2006.

[136] S. Simpson and E. Zurek, "Substituted benzene derivatives on the cu(111) surface," *The Journal of Physical Chemistry C*, vol. 116, pp. 12636–12643, June 2012.

[137] N. Kepija, Y.-Q. Zhang, M. Kleinschrodt, J. Bjrk, S. Klyatskaya, F. Klappenberger, M. Ruben, and J. V. Barth, "Steering on-surface self-assembly of high-quality hydrocarbon networks with terminal alkynes," *The Journal of Physical Chemistry C*, vol. 117, pp. 3987–3995, Feb. 2013.

[138] A. D. Jewell, S. M. Simpson, A. Enders, E. Zurek, and E. C. H. Sykes, "Magic electret clusters of 4-fluorostyrene on metal surfaces," *The Journal of Physical Chemistry Letters*, vol. 3, pp. 2069–2075, Aug. 2012.

[139] D. Riedel, M.-L. Bocquet, H. Lesnard, M. Lastapis, N. Lorente, P. Sonnet, and G. Dujardin, "Selective Scanning Tunnelling Microscope Electron-Induced Reactions of Single Biphenyl Molecules on a Si(100) Surface," *Journal of the American Chemical Society*, vol. 131, pp. 7344–7352, June 2009.

[140] M. Lastapis, M. Martin, D. Riedel, L. Hellner, G. Comtet, and G. Dujardin, "Picometer-Scale Electronic Control of Molecular Dynamics Inside a Single Molecule," *Science*, vol. 308, pp. 1000–1003, May 2005.

[141] M. Amft, S. Lebègue, O. Eriksson, and N. V. Skorodumova, "Adsorption of Cu, Ag, and Au atoms on graphene including van der Waals interactions," *Journal of Physics: Condensed Matter*, vol. 23, p. 395001, Oct. 2011.

APPENDICES

Appendix A

Supporting Information for Chapter 4

A.1 Experimental observations

A.1.1 Formations of Hexamers at Different Coverage

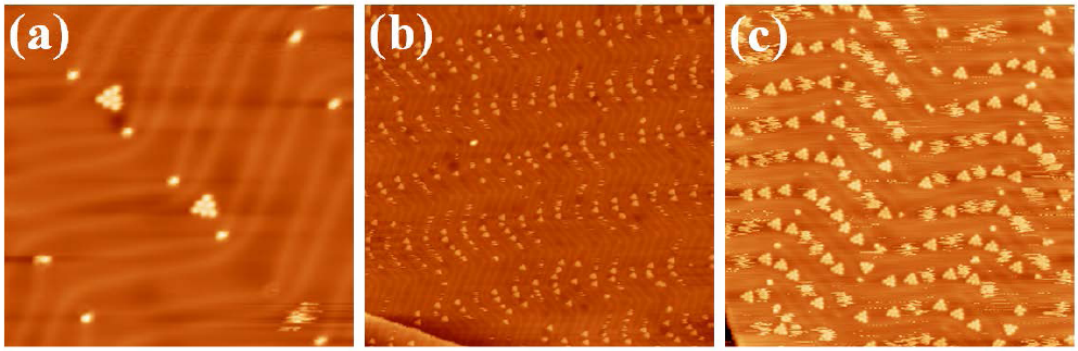

Figure A.1: STM images of the surface at different molecular coverage. (a) Coverage is 0.01 ML (35 nm × 35 nm, 1.0 V, 50 pA). (b) Coverage is 0.1 ML (120 nm × 120 nm, 0.8 V, 30 pA). (c) Coverage is 0.01 ML (60 nm × 60 nm, 1.0 V, 30 pA).

As illustrated in Figure A.1, magic clusters can form even when the molecular coverage is as low as 0.01 ML. When the coverage increases, more hexamers appear on the substrate and with robust retention of the underlying internal structure. This coverage-independent phenomenon indicates that due to the high temperature annealing the magic clusters represent molecular equilibrium structures.

A.1.2 Stability Against Electrical Pulsing

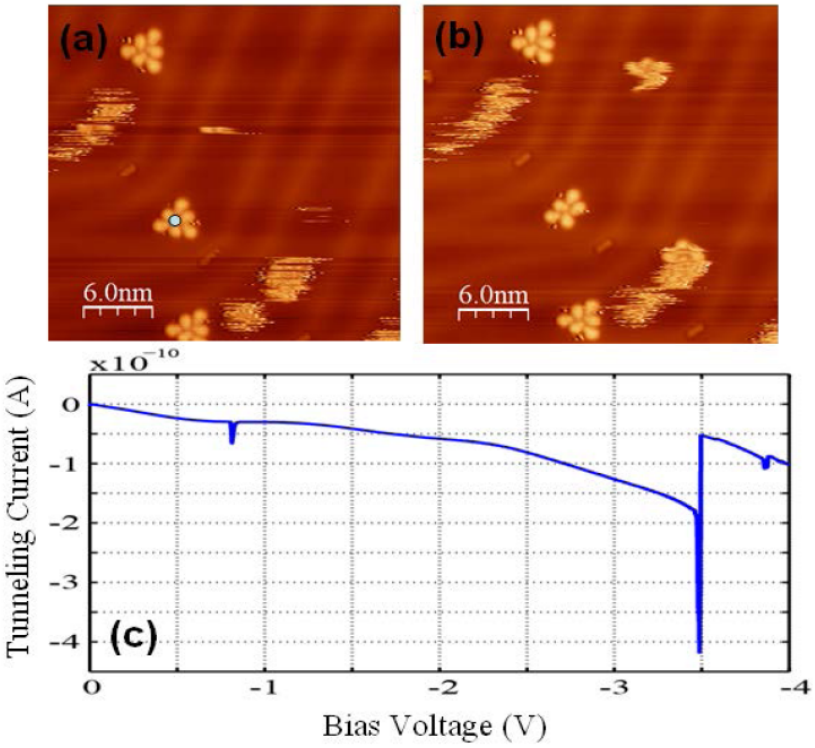

Figure A.2: (a) STM images show the hexamer before applying negative voltage pulse. (b)The pentamer after pulsing. (c)The recorded tunneling current vs. voltage of pulse.

We also note that the hexamer complex is surprisingly stable against electric fields in the tunneling junction created by pulsing the molecules with the STM tip. At first the tip was placed at a fixed position over a peripheral molecule, as highlighted by a dot in Figure A.2a. No dissociation events were observed when applying a negative bias voltage smaller than -2.8 V in magnitude. However, at sample bias $V_s > -3$ V, the target molecule disassociated from the cluster (Figure A.2c). The remaining pentamer maintained its structure when imaged by the STM, and in fact the core was largely unchanged from the hexamer (Figure A.2b). Dissociation events in the chosen voltage range could be efficiently induced only at negative tip bias, suggesting that the reaction is mediated by a transient anionic specie formed by electron attachment to the LUMO of the molecule, in analogy to the behavior of biphenyl on Si(100) [139, 140]. The central three molecules could not be dissociated until the hexamer is broken down by larger voltage pulses.

A.1.3 Manipulation of Hexamer, Dissociation and Aggregation

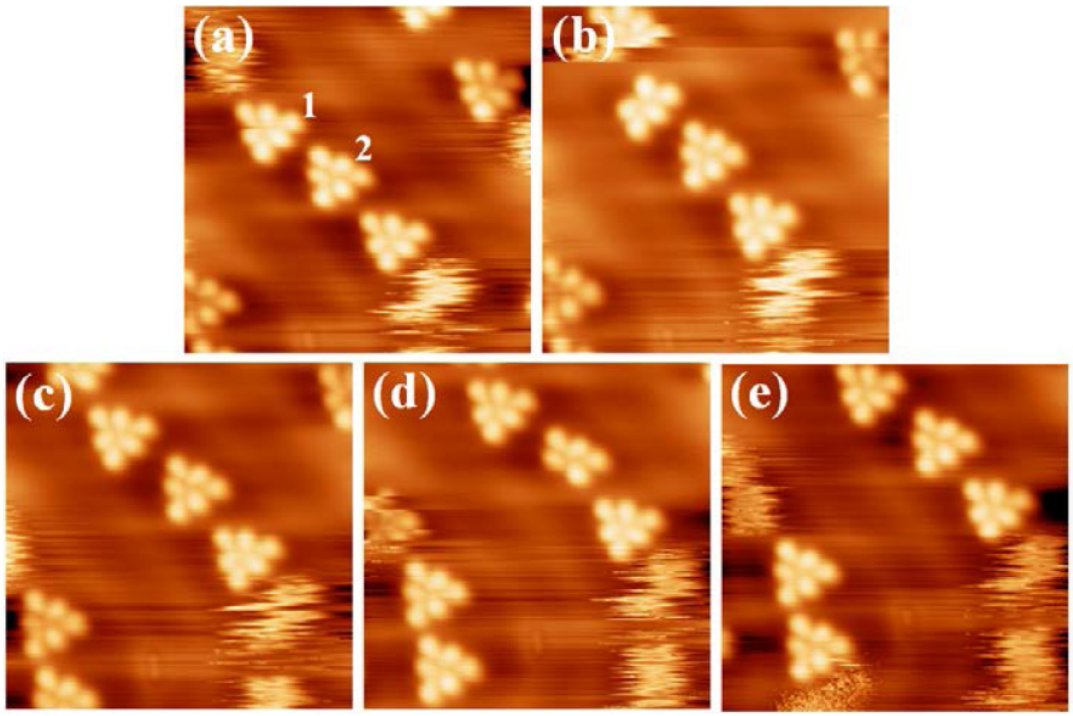

Figure A.3: Manipulation of hexamers. (a) STM image shows several hexamers. (b) After removing one peripheral molecule from cluster 1. (c) Cluster 1 absorbs one molecule and forms a stable hexamer again. (d) After removing one peripheral molecule from cluster 2. (e) Cluster 2 absorbs one molecule and forms a stable hexamer again. Image sizes are 12 nm $\times$ 12 nm. All the images were acquired under the same tunneling condition (0.5 V, 20 pA).

To further confirm that hexamers are the most stable structures, we performed molecular manipulation experiments. We removed one peripheral phenylacetylene molecule from cluster 1 (Figure A.3a and b) and then scanned the imaged region continuously. Over time, the pentamers absorb individual molecules to form hexamers. This manipulation is highly reproducible and independent of cluster position (Figure A.3c to A.3e). Notice that cluster 1 and 2 have different chiralities (clockwise (C) and anticlockwise (A) hexamers). The chiral character is induced by the surface-molecule interactions and is an aspect of self-assembly that may also have a degree of tunability given the appropriate choice of the surface structure.

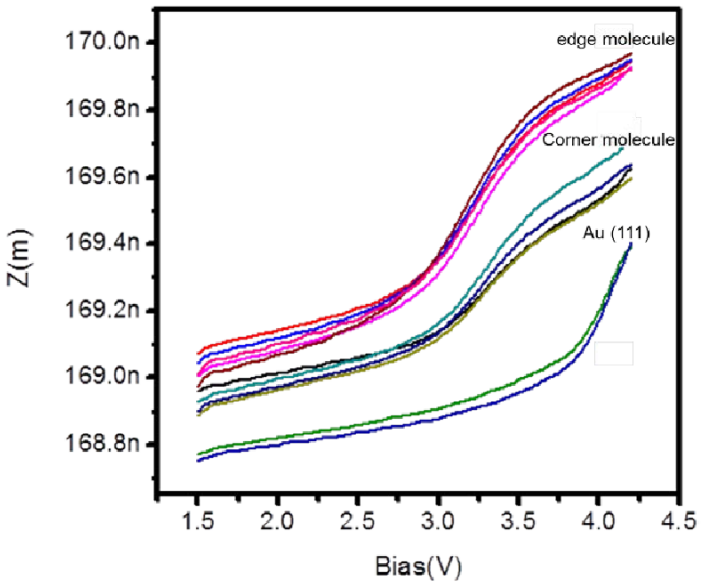

Figure A.4: Raw data of the Z/V spectra at different molecule positions (corner and edge) of the hexamer and bare Au surface.

A.1.4 Z–V Spectra of the Hexamer

The electronic properties of the hexamer were investigated by measuring the distance-voltage (Z–V) spectra, which register displacement of the tip relative to the surface with increasing bias. When a resonance, such as a molecular state, falls into a tunneling window, an abrupt increase of the tunneling conductance takes place, which results in a large step in the z-displacement (see Figure A.4). We can see that the spectra at different molecule positions are quite reproducible.

A.2 Theoretical Calculations

A.2.1 Binding Energy for Phenylacetylene Clusters in Gas Phase

We computed structures and binding energies for a variety of cluster sizes in gas phase using PBE and vdW-DF. In the cluster 7', the hexamer was constrained within its plane, while the molecule pointing out of that plane was relaxed with 3D freedom. The binding energy is calculated as the difference between the cluster's total energy and the single phenylacetylene molecule's total energy times the number of molecules in that cluster. Figure A.5 shows the different cluster geometries (Figure A.5a) and the computed binding energy (Figure A.5b).

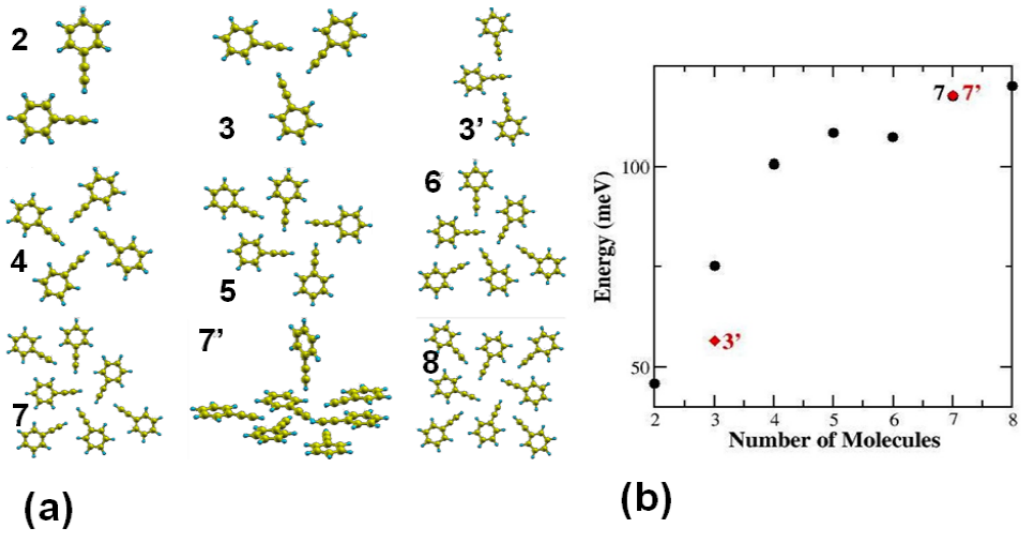

Figure A.5: Gas phase binding energy study with different clusters. (a) Relaxed structures for gas-phase cluster. (b) Binding energy of each cluster.

A.2.2 Binding Energy of the Hexamer in Six Different Configurations

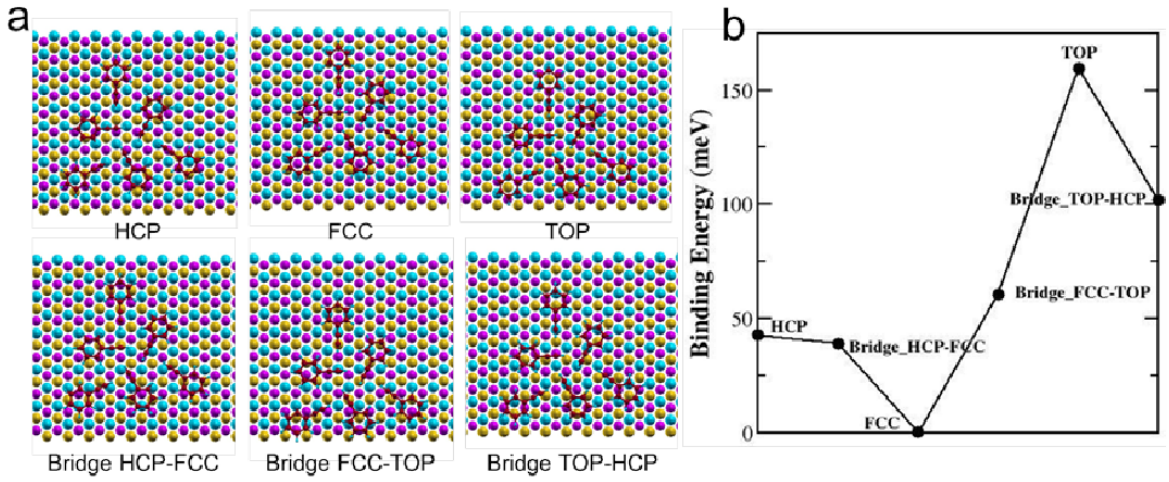

Figure A.6: Binding energy of hexamer in different configurations. (a) Six different configurations. (b) Binding energy of each configuration. Color code for Au atoms: yellow, top layer; blue, hcp layer; purple, fcc layer. There are 4 layers Au being used in our calculations.

Six different configurations for the hexamer on Au(111) were investigated. They are fcc, top, hcp, bridge-hcp-fcc, bridge-hcp-top, and bridge-top-hcp (see Figure A.6a). The binding energy for each configuration (see Figure A.6b) was computed using PBE and the DFT-D2 approach of Grimme to the long-range interactions. The $C_6(R_0)$ coefficients for H, C and Au were 0.14 J nm^6/mol (1.001 $\mathring{A}$), 1.75 J nm^6/mol (1.452 $\mathring{A}$), 40.62 J nm^6/mol (1.772 $\mathring{A}$), respectively; the values for H and C were taken from Grimme's original paper [102] whereas those for Au were taken from Ref. [141] Each configuration consisted of a hexagonal unit cell with dimensions 29.7 $\mathring{A}$ x 29.7 $\mathring{A}$ x 27.6 $\mathring{A}$, with the hexamer placed on top of a Au(111) slab made of 4 layers and at a distance of 3.68 $\mathring{A}$. The unit cell dimensions ensure that the periodic images of the hexamer are about 9 $\mathring{A}$ apart in the x- and y-direction, and about 17 $\mathring{A}$ apart in the z-direction. We used the projector augmented-wave pseudopotentials (PAW) [49] with an energy cutoff of 400 eV, the Γ point and dipole corrections. The calculations were carried out with the Vienna Ab-initio Simulation Package (VASP) [124]. The structures were not relaxed, and thus the energy barrier showed in Figure A.6b is probably an overestimation.

Appendix B

Supporting Information for Chapter 5

B.1 Experimental Observations

B.1.1 Variable Temperature Observation of Phenylacetylene on Au(111) Substrate

From our earlier studies, the adsorbed phenylacetylene molecules are flat-lying on the Au(111) surface and arrange themselves into supramolecular hexamer clusters that can be reliably imaged at 28 K [76]. The binding energy of each molecule to the Au(111) surface in such a cluster is small, leading naturally to facile diffusion at 85 K. This fact can be further supported by temperature dependent STM images shown in Figure B.1. The hexamers composed by flat-lying phenylacetylene start to diffuse at 32 K and the STM image becomes fuzzy at about 50 K. Thus we believe that the fuzzy image acquired at 85 K demonstrates the significant mobility of the flat-lying phenylacetylene molecules on the Au(111) surface.

B.1.2 Creating the Ordered Phase by Scanning with Positive Voltages

As seen in Figure B.2, a clear ordered structure emerges after scanning the surface with positive voltage. Furthermore, the ordered island keeps growing during the continuous scanning, due to the electron-induced molecular transformation from flat-lying phenylacetylene to upright styrene-derivative, as described in the main text.

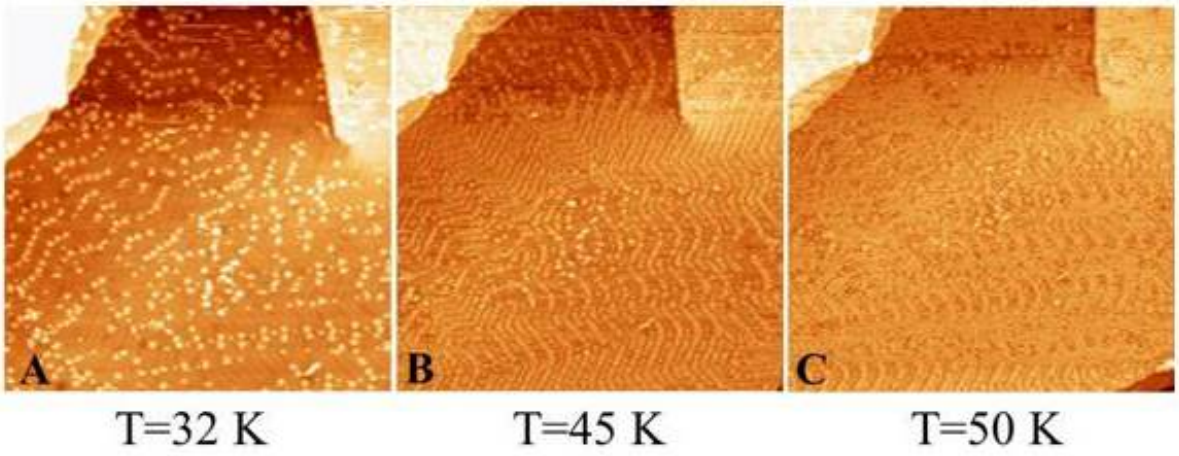

Figure B.1: Topographic STM images under various temperatures. Scanning size is 200×200 nm^2, bias voltage is +1 V and the tunneling current is 50 pA.

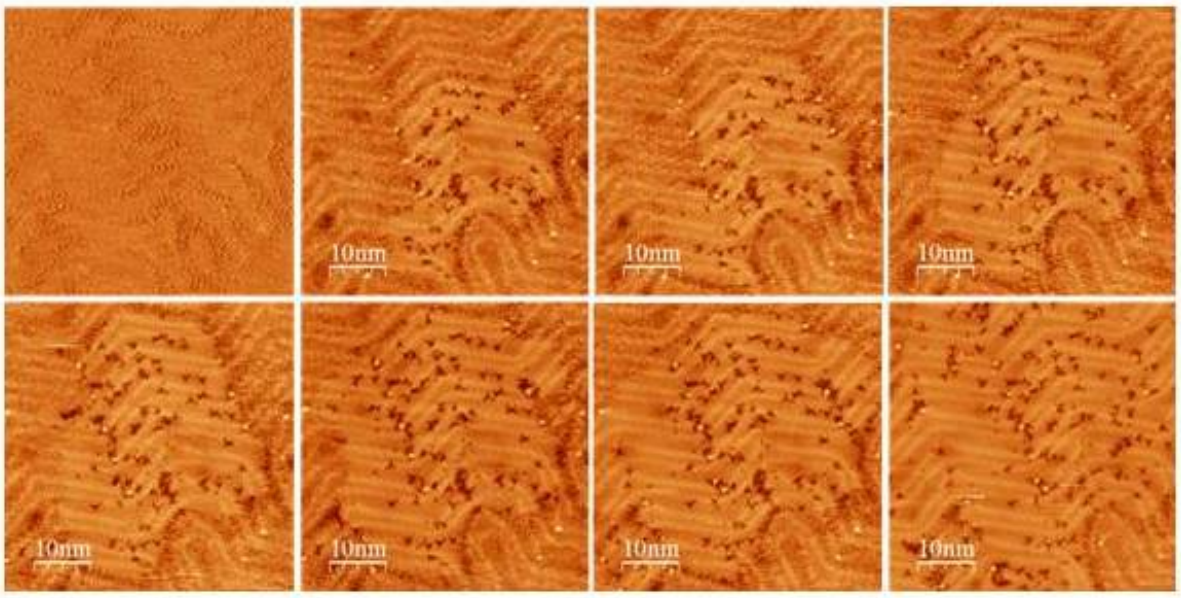

Figure B.2: Topographic STM images during the continuous scanning. Bias voltage is +1.0 V and the tunneling current is 30 pA.

B.1.3 The Manipulation of the Defects Embedded in the Self-Assembled Layer

As described in the main text, the ordered structure is composed of upright styrene-derivative molecules, while the embedded defects within the self-assembled layer are attributed to the flat-lying phenylacetylene molecules. Therefore, the achieved various manipulations of the defects, including motion, emergence, and disappearance (Figure B.3), represent reactions in a single molecular layer.

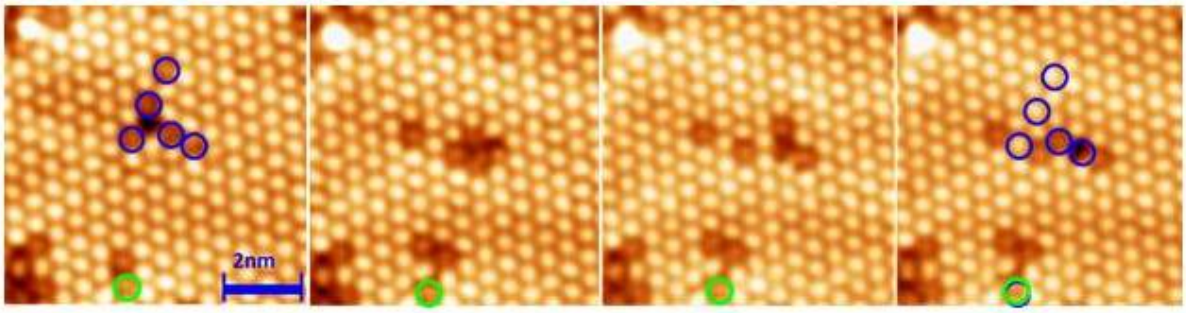

Figure B.3: A series of subsequent images showing random manipulation of various defects within the ordered structure. The tip was scanned at a bias of +1 V and a current of 30 pA.

B.1.4 Size Dependence of the Erasing Process

We studied the disassembly process of different-size ordered structures (Figure B.4b) using a fixed pulse voltage (−0.5 V). We found that the time needed to erase an island of a given area scales linearly with its size (Figure B.4a). Thus, the net electron fluence scales linearly with the number of molecules, identifying single-electron kinetics with 6.3×10^{-7} molecule per electron.

B.2 Theoretical Calculations

B.2.1 Geometry Relaxation

The optimized structures for a single molecule on Au(111) are shown in Figure B.5. For phenylacetylene on Au(111), we studied 12 different configurations. After relaxation, the molecules did not change significantly their relative orientation at the substrate. The same is not true for the styrene and phenylvinylidine derivatives on Au. For each, we studied 4 different configurations, which are the same as considered by Ford *et al.* [117]. For the styrene derivative,

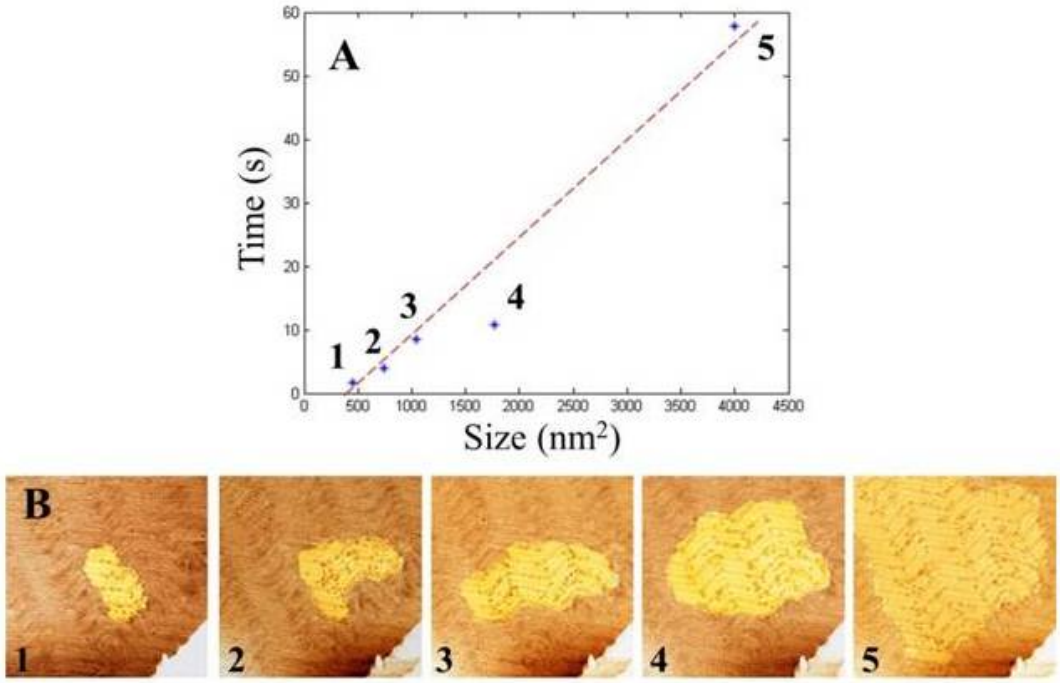

Figure B.4: Size dependence of the erasing process. (a) A plot showing the time needed to erase an ordered molecular island *vs.* the island size. (b) The topographic image of the molecular island to be disassembled.

all the structures are "not stable", except for the TOP structure. By "not stable" we mean that relaxation changed the relative orientation of the molecule with respect to the substrate. In particular, the bridge (BR) and HCP orientations become a new structure, which we called BR-A, characterized by having the middle of the C–C ethylene axis placed above an Au atom of the third layer. A similar transformation happens to the FCC structure upon relaxation, with the middle of the C–C ethylene axis placed above a Au atom of the second layer; we called this new structure BR-B. Ford *et al.* [117] did not discuss whether some structures were not stable, but only included binding and interaction energies for the TOP structure. For phenylvinylidine, HCP and FCC are metastable, whereas TOP and BR become FCC after relaxation. Ford *et al.* [117] also found that the BR structure becomes FCC, whereas the TOP configuration is metastable, albeit considerably less stabilized than FCC or HCP.

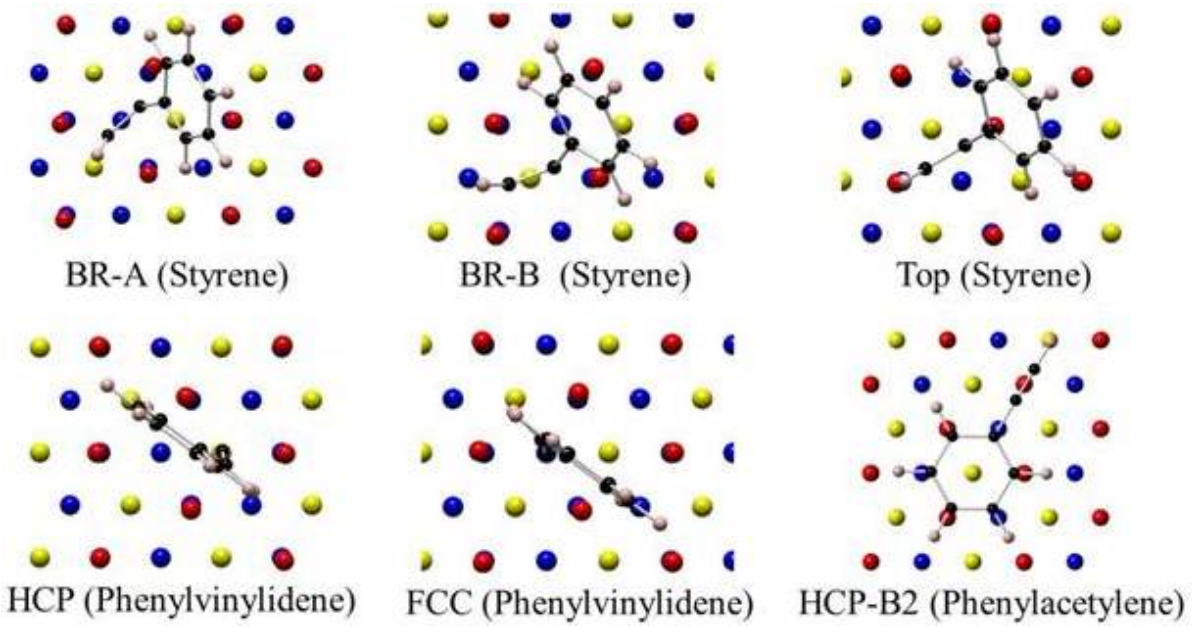

Figure B.5: Relaxed structural models of Styrene-derivative, Phenylvinylidene and Phenylacetylene on Au. Color code: 1st layer, red; 2nd layer, yellow; 3rd layer, blue.

Once the structures were relaxed, the binding energy ΔE, and the interaction energy ΔI were computed. $\Delta E = E_{tot} - E_{Au} - E_{mol}$, where E_{tot}, E_{Au} and E_{mol} are the energies of the relaxed total system (*i.e.*, the system comprised of the molecule attached to the Au substrate), relaxed Au substrate and relaxed molecule. $\Delta I = E_{tot} - E_{Au} - E_{mol}$, where E_{Au} and E_{mol} are the energies of the Au substrate and molecule with the same configurations they have in the total system. To compute E_{Au} and E_{mol} we simply extracted the Au substrate or the molecule

from the total system and computed their energies without any relaxation. Table B.1 shows the binding and interactions energies of all the structures studied.

Table B.1: Binding energies and interaction energies for all the relaxed structures. Only the energies of stable structures are included.

Molecule	Surface site	Binding ΔE (eV)	ΔI (eV)
Styrene derivate	BR-A	-0.235	-3.140
	BR-B	-0.090	-2.894
	TOP	-0.093	-2.335
Phenylvinylidene	HCP	-0.253	-2.859
	FCC	-0.421	-2.997
Phenylacetylene	BR-A1	-0.061	-0.072
	BR-A2	-0.064	-0.080
	BR-B1	-0.050	-0.060
	BR-B2	-0.065	-0.083
	FCC-A	-0.037	-0.052
	FCC-B1	-0.039	-0.050
	FCC-B2	-0.066	-0.092
	HCP-A	0.021	-0.091
	HCP-B1	-0.044	-0.054
	HCP-B2	-0.069	-0.093
	TOP-A	-0.042	-0.054
	TOP-B	-0.017	-0.025

B.2.2 Projected Density of States (PDOS)

We can see from the PDOS calculation (Figure B.6) that when placed onto the gold surface, both the phenylvinylidene and styrene-derivative have their HOMOs significantly broadened and approaching the Fermi level of the Au surface. This calculation explains the small energy threshold for the disassembly reaction.

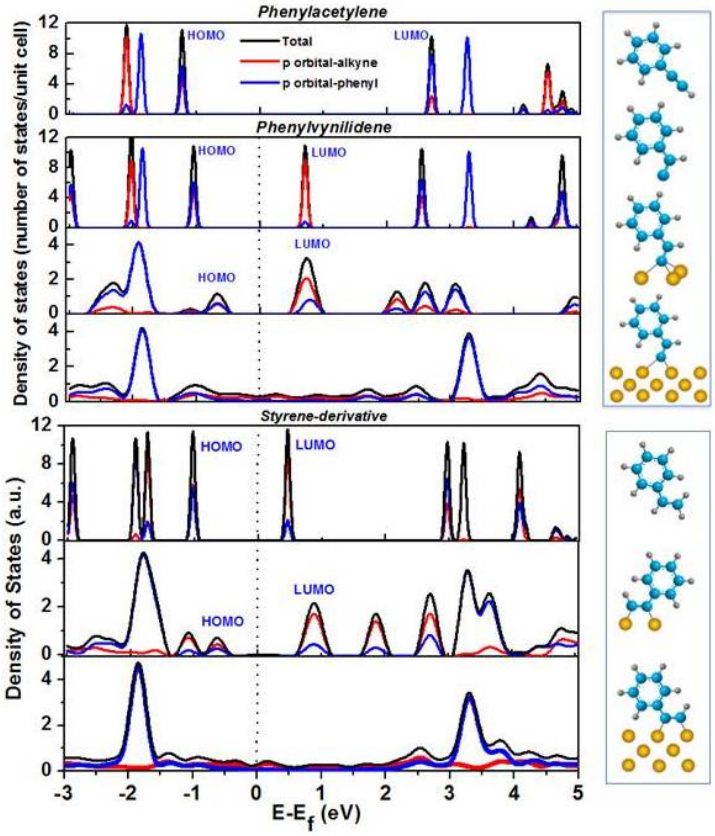

Figure B.6: Calculated PDOS for various molecular configurations. (top to bottom): gas-phase phenylacetylene, gas-phase phenylvinylidene, phenylvinylidene with three gold atoms, phenylvinylidene on four layers of Au, gas-phase styrene-derivative, styrene-derivative with three gold atoms, and styrene-derivative on four layers of Au. The seven corresponding structures are exhibited at the right side. All PDOS plots are aligned according to deep filled states.